

Pore Scale Processes Associated with Subsurface CO₂ Injection and Sequestration

Carl I. Steefel¹, Sergi Molins¹, David Trebotich²

¹*Earth Sciences Division*

²*Computational Research Division*

Lawrence Berkeley National Laboratory

Berkeley, California 94720, U.S.A.

cisteefel@lbl.gov smolins@lbl.gov DPTrebotich@lbl.gov

INTRODUCTION

The injection of CO₂ into the Earth's subsurface drives the fluid-rock system into "far-from-equilibrium" conditions, which means that the fluxes that return the system to equilibrium are nonlinearly related to the generalized driving forces (e.g., chemical affinities and gradients in the fluid pressures and chemical potentials). The nonlinear response results in emergent structures and self-organization (Prigogine 1968, 1980; Ortoleva 1994; Lasaga 1998; Jamtveit and Meakin 1999), of which the reactive infiltration instability is a well-known example in the Earth Sciences that is directly applicable to CO₂ injection and caprock integrity (Ortoleva et al. 1987; Hoefner and Fogler 1988; Steefel and Lasaga 1994; Steefel and Maher 2009). Flow, solute transport, colloid transport, mineral dissolution and mineral precipitation combine within the mechanical framework of the porous medium to generate precipitate structures in individual pores correlated over many thousands to millions of pores, and immiscible fluid structures with fractal geometry over scales from millimeters to kilometers (Feder 1988). The focus in this chapter is on processes, emergent and otherwise, taking place at the pore scale, defined here as the scale where individual grains and fluid interfaces can be resolved.

The chief focus of research in recent years has been to improve the understanding of the nonlinear dynamics specifically associated with biogeochemical and microbially induced processes coupled to physical processes such as flow and diffusion at the pore scale. When coupled, whether in field-scale applications, bench-scale experiments, or in models, emergent behavior may result, including changes in permeability, diffusivity, and reactivity. The pore scale is an important scale to analyze these emergent behaviors given that it provides the architecture within which the smaller scale (nano and molecular scale) processes occur. For the individual processes to interact, transport is typically necessary and the resulting behavior is not predictable from consideration of the individual processes alone. The continuum scale, in which the detailed properties of the pore structure are averaged in some fashion, is an abstraction that may not preserve all of the dynamics at the micro-scale.

The final equilibrium states and the time scales to reach equilibrium, which are critical to meaningful predictions of system behavior, cannot be assessed in the absence of proper governing equations applicable to large scales that are rooted in correct descriptions of molecular-to-pore scale processes. The interest is on how bulk properties such as permeability, diffusivity and reactivity can be related back to pore scale and smaller phenomena, as well as how they change as a result of the stresses associated with CO₂ injection.

Pore scale structure and CO₂ sequestration

Natural subsurface materials have their own pore scale architecture that regulates how physical and chemical processes are coupled. Pore spaces are filled with brine (water) and/or CO₂ and are bordered by a range of solid phases that may be reactive (Fig. 1). While cations for carbonate formation are generally present in the brine, their concentrations are typically not high enough in the brine to precipitate all of the CO₂ that is locally present. Another important effect has to do with the fact that gaseous or supercritical CO₂ dissolves in the aqueous phase to form carbonic acid according to the reaction

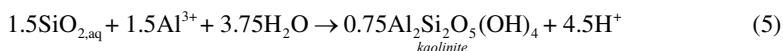
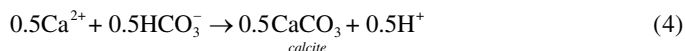


thus lowering the pH of the aqueous phase as the carbonic acid dissociates to the bicarbonate ion



Since the solubility of all carbonate phases is higher at low pH than at high or circumneutral pH, this effect tends to reduce the amount of carbonate that can be formed. Formation of a significant mass of carbonate, therefore, requires that the pH be raised, generally as a result of the dissolution of cation and alkalinity-bearing phases (e.g., silicates). Within the pore structure of the subsurface materials, therefore, transport effects become important insofar as cations and alkalinity must be moved from dissolving phases to nucleation and growth sites, whether in pore throats or pore bodies (Fig. 1). At high CO₂ (and low water) saturation, transport within the aqueous phase may become slower due to the increased tortuosity, even though water serves as the wetting phase providing a reactive medium adjacent to the mineral surfaces. An additional effect is that a small amount of water (up to 5%) may dissolve in the supercritical CO₂ phase, thus potentially leading to drying out in those portions of the system that experience high CO₂ fluxes (McGrail et al. 2009). This has been observed to lead to halite precipitation, which can have the effect of reducing permeability in the near well-bore regions where the CO₂ flux is the highest (e.g., Muller et al. 2009). Additional discussion of CO₂ injection and sequestration impacts can be found in Jun et al. (2013).

A generic reaction in which silicates dissolve under acidic conditions and precipitate carbonates can be written using Ca-bearing plagioclase (An₅₀, or labradorite), calcite, and kaolinite as model phases (Fig. 1):



where the reaction has been balanced on the Ca²⁺ and Al³⁺ ions released from the plagioclase dissolution. Note that while it is customary in geochemistry textbooks to write reactions as perfectly balanced between dissolving and precipitating phases, in nature (or in numerical reactive transport models) this is rarely the case because of the effects of transport and kinetics (Brimhall 1979; Steefel and Lichtner 1994). Note also that the plagioclase dissolution, in addition to releasing the calcium ion needed to precipitate the calcite, provides alkalinity and thus consumes protons. It should be noted in this regard that not all Ca-bearing minerals contribute alkalinity upon dissolution (the sulfate-bearing minerals gypsum and anhydrite are good examples), so their tendency to drive carbonate precipitation is not as great. In general, the dissolution of silicate minerals containing metals that can readily form carbonates (Ca²⁺, Mg²⁺, and Fe²⁺) also provide alkalinity to neutralize the carbonic acid associated with CO₂.

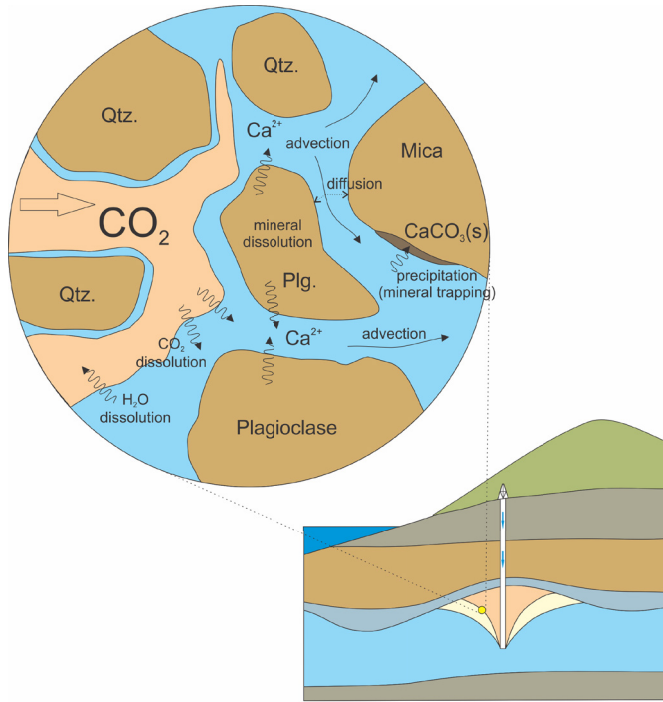


Figure 1. Schematic representation of chemical and physical processes associated with CO₂ injection and sequestration at the pore scale (brine is in blue). Qtz = quartz, Plg = plagioclase.

It should also be readily apparent from what we know of the pore architecture, as represented for example as in Figure 1, that the various phases dissolving and precipitating, as well as the CO₂ itself, need not be strictly co-located. While carbonate may form directly on the dissolving phase, in other cases there can be a significant separation in space between the neoformed carbonate and the metal and alkalinity source, particularly under acidic conditions (Daval et al. 2009). In part this may be the result of the tendency for nucleation of carbonate phases preferentially on some mineral surfaces versus others because of the lower interfacial energy of these phases (De Yoreo et al. 2013, this volume). This implies that the physical processes of flow and transport at the pore scale are likely to be important in mediating reaction rates, which implies in turn that pore scale CO₂ sequestration is a mesoscale rather than a strictly molecular or microscale problem. An example of the pore structure in a sandstone imaged with X-ray microtomographic techniques and the associated flow calculated using the Navier-Stokes equation is shown in Figure 2. Distributions of CO₂ may be even more heterogeneous (Sato et al. 2011), separated in some cases from the dissolving phases by centimeters and even meters (i.e., well beyond the pore scale that we address here).

Pore scale methods

An improved understanding of the pore scale dynamics associated with CO₂ injection and sequestration require an advanced set of experimental, imaging and modeling tools. The rapidly developing field of 3D imaging techniques (X-ray, neutron, and magnetic resonance) allow for the characterization and observation of dynamic geological and hydrological processes on unprecedented temporal and spatial resolutions (Carlson 2006). Among these three techniques, X-ray computed tomography has been most widely used for 3D imaging of geologic materials

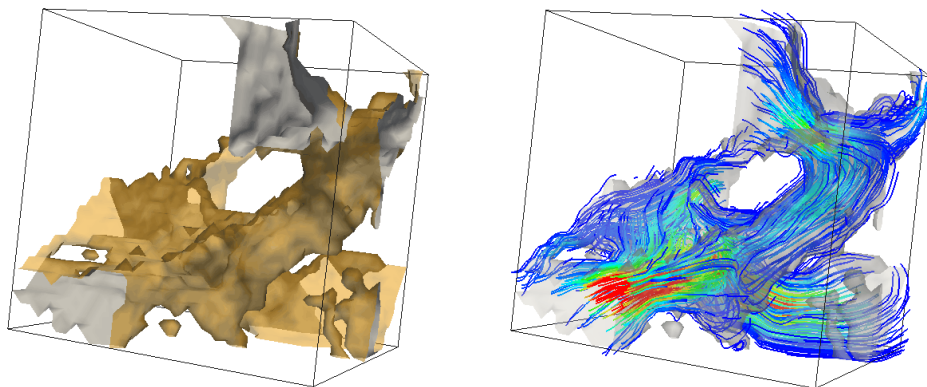


Figure 2. Image of a set of connected pores from X-ray microtomographic imaging (300 μm each side), with calculation of the flow streamlines and their magnitude (from Molins et al. 2011).

(Mees et al. 2003; Wildenschild and Sheppard 2013). Another important technique is Small Angle Neutron Scattering (SANS), which although not a 3D microtomographic approach, is useful in detecting changes in pore size at scales much smaller than what can be imaged with the tomographic methods. Complementary 2D imaging of CO_2 invasion dynamics at the pore scale can be carried out using two-dimensional optically transparent pore networks called “micromodels.”

To complement the imaging of CO_2 injection, a second equally important requirement is the use of pore-scale reactive transport modeling tools. Pore scale models differ from continuum models in that each of the phases involved and their interfaces must be resolved explicitly. High resolution and extreme computing capabilities are necessary. Methods employed include particle methods, lattice Boltzmann or Direct Numerical Simulation. Pore networks are also been used, especially in multiphase applications.

Organization of chapter

In what follows, the physics of single phase flow (CO_2 dissolved in brine) and multiphase flow (CO_2 and brine) are briefly discussed. Geochemical processes operating at the pore scale are then reviewed, particularly those that are relevant to the emergent processes that are the focus of the remainder of the chapter. Pore scale experimental and characterization approaches are summarized, followed by a discussion of modeling approaches and results specific to this scale and architecture. Finally, the set of emergent behaviors associated with pore scale physical and chemical processes are reviewed. Ultimately, the focus is on insights from the pore scale that can be used to develop phenomenological laws that will provide an improved predictive capability for CO_2 injection and sequestration at the porous-continuum scale.

PHYSICS OF SINGLE PHASE FLOW AT THE PORE SCALE

Owing to its relatively high solubility in water, dissolution of CO_2 into the pore solution can contribute significantly to its trapping in the subsurface both in the short and long term (DePaolo and Cole 2013, this volume). As a dissolved component in the aqueous phase, the fate of CO_2 in the subsurface will depend on the flow of water in the pore space. In particular, transport in the aqueous phase mediates dissolution and precipitation processes driven by elevated CO_2 concentrations and resulting low pH conditions by enabling chemical transformations in solution and at mineral surfaces.

Single-phase aqueous flow in the pore space is subject to inertial, viscous and other body forces such as gravity ($\mathbf{f}_b = \mathbf{g}$). Inertial forces have their origin in the convective acceleration of the fluid as it flows through the tortuous pore space. Viscous forces originate in the friction between water molecules and are responsible for the dissipation of energy. Given the small compressibility of water, in most subsurface conditions, the incompressible Navier-Stokes equations can be used to accurately describe aqueous flow via the conservation of momentum and mass, respectively

$$\rho \left(\frac{\partial \mathbf{u}}{\partial t} + (\mathbf{u} \cdot \nabla) \mathbf{u} \right) = -\nabla P + \mu \nabla^2 \mathbf{u} + \mathbf{f}_b \tag{6}$$

$$\nabla \cdot \mathbf{u} = 0 \tag{7}$$

where \mathbf{u} is the fluid velocity, ∇P is the pressure gradient, ρ is the fluid density, μ is the dynamic viscosity. The left hand side of Equation (6) represents the inertial terms, while the right hand represents the divergence of the stress and the body forces.

The ratio between inertial and viscous forces is expressed by the Reynolds number, Re :

$$Re = \frac{|u|l}{\nu} \tag{8}$$

where $|u|$ is the fluid velocity magnitude, ν is the kinematic viscosity, and l is a characteristic length of the porous medium (e.g., average grain size). At low Reynolds numbers (i.e., $Re \ll 1$), inertial forces can be neglected and Stokes flow is valid. Under steady-state conditions, the Navier-Stokes equation simplifies to the Stokes equation

$$\nabla P = \mu \nabla^2 \mathbf{u} + \mathbf{f}_b \tag{9}$$

which is solved again together with Equation (7).

Even when inertial forces are not negligible, consideration of viscous forces is necessary to account for energy dissipation. In no-slip flow, the velocity of the fluid is zero at the mineral grain surface and a thin region forms around mineral grains where viscosity dominates. This boundary layer generates most of drag exerted on the mineral grain (Fig. 3).

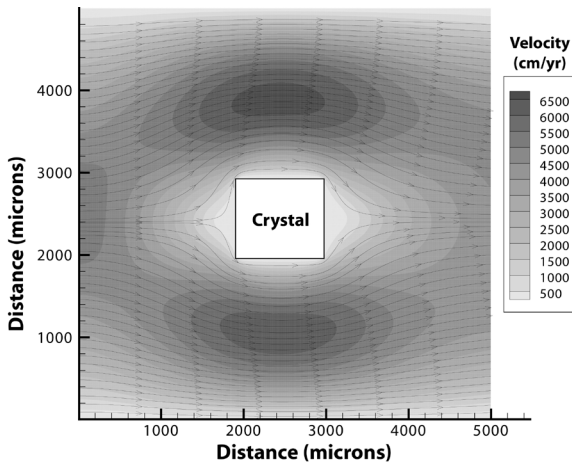


Figure 3. 2D pore scale simulation of Navier-Stokes flow past a crystal using the Chombo software.

PHYSICS OF MULTIPHASE FLOW AT THE PORE SCALE

The injection of CO₂ in the subsurface clearly involves multiphase flow. A recent review of modeling of pore scale multiphase fluid flow in fractured and porous media devoted to general applications, including the vadose zone and hydrocarbon reservoirs, is given by Meakin and Tartakovsky (2009) along with a thorough general description of the fundamentals of multiphase flow at the pore scale. Here, the basic concepts of multiphase flow applicable at the pore scale are reviewed, focusing on the CO₂-brine system.

The injection of CO₂ in the subsurface involves the displacement of a wetting phase (brine) that initially occupies the pore space by a non-wetting phase (supercritical CO₂), a drying process. The resulting dynamic system is characterized by CO₂-brine fluid-fluid interfaces and the contact angles of these interfaces at the mineral surfaces that evolve with time. The concept of capillary surface is commonly employed to describe the interface between two fluids such as CO₂ and brine. Implicit in the concept of surface is the assumption of a sharp or infinitely thin transition between fluids. Due to the surface tension, a pressure discontinuity exists at this fluid-fluid interface. This pressure discontinuity or capillary pressure P_c is related to the interfacial tension γ_{wc} and the surface mean curvature ($1/r_1+1/r_2$) through the Young-Laplace equation:

$$P_c = P_{CO_2} - P_{brine} = \gamma_{wc} \left(\frac{1}{r_1} + \frac{1}{r_2} \right) \quad (10)$$

The curvature of this interface controls the capillary pressure, which dominates over viscous forces under typical conditions. At the fluid-fluid-solid interface, the contact or wetting angle between phases at equilibrium under static conditions on an ideal surface is given by

$$\cos\theta = \frac{\gamma_{sc} - \gamma_{sw}}{\gamma_{wc}} \quad (11)$$

where γ_{sc} is the interfacial tension between the solid and the CO₂, and γ_{sw} is the interfacial tension between solid and brine. In the dynamic conditions driven by CO₂ injection, Equation (11) is not applicable and the contact angle depends on displacement of the interface (e.g., whether CO₂ is displacing brine or the opposite), the velocity of this moving interface at the solid surface, and the direction of motion of the fluid-fluid-solid contact line. Capillary pressure variations may also arise from the mineral contact angle heterogeneity inherent in geological formations (Ellis and Bazylak 2012, 2013). Mineral surfaces are not perfectly smooth or chemically homogeneous, which may explain differences between the advancing (θ_a) and receding (θ_r) contact angles that are observed. This difference is commonly referred to as the contact angle hysteresis. Hysteretic behavior also exists because of the breakup in symmetry once the non-wetting fluid goes from small to large pore versus the opposite (ink-bottle effect). Empirical models for contact angle hysteresis exist (de Gennes 1985), but recent experimental studies with scCO₂ on silica surfaces (Fig. 4) suggest also a time-dependent evolution of the wettability (Jung and Wan 2012; Kim et al. 2012).

The invasion of a non-wetting phase (e.g., $c = CO_2$) in a saturated porous medium can be characterized by the capillary number ($Ca = u_c \mu_c / \gamma_{wc}$), the viscosity ratio ($M = \mu_c / \mu_w$) (and the Bond number ($Bo = \Delta\rho g l^2 / \gamma_{wc}$), where $\Delta\rho$ is the density difference (Lenormand et al. 1988; Ewing and Berkowitz 1998; Blunt 2001). When viscosity forces dominate (e.g., near an injection point) and the viscosity ratio is high, stable front propagation is expected. However, when that is not the case, displacement leads to unsteady front propagation. In this case, capillary, viscous or gravity fingering may be observed depending on whether capillary forces (small Ca), viscosity of the brine (small M) or gravitational forces dominate, respectively (Lenormand et al. 1988; Ewing and Berkowitz 1998; Blunt 2001). In CO₂ sequestration scenarios, the displacement process is considered unstable due to the unfavorable viscosity ratio between the invading

scCO₂ and the resident brine (log M < 0) (e.g., Zhang et al. 2011; Wang et al. 2013). After CO₂ injection has stopped, buoyant rise of the CO₂ continues (Fig. 5), capillary forces become dominant and non-wetting CO₂ bubbles and stringers that are not physically connected are left behind, an effect referred to as capillary trapping (Fig. 5). The ratio of buoyancy to viscous forces can also be expressed as a function of Ca and Bo.

Multiphase interfacial processes and contact angles relevant for CO₂ sequestration are reviewed in detail in three other chapters in this volume and will not be discussed in depth here. Hamm et al. (2013, this volume) reviews the current knowledge of interfacial tension between brine and CO₂, while Tokunaga and Wan (2013, this volume) reviews the current knowledge of mineral surface wettability under relevant sequestration conditions.

Although a sharp interface is often assumed, real CO₂-brine interfaces may not necessarily be accurately described as infinitely thin at the pore scale. Diffuse-interface theories replace the sharp interface with a continuous variation of an order parameter (e.g., density). Surface

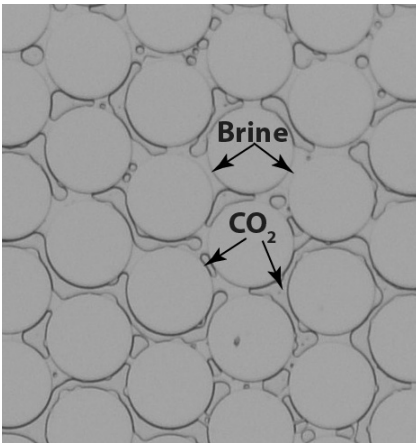


Figure 4. Photograph of a micromodel experiment at high supercritical CO₂ saturation showing isolated water (brine) droplets. The microscopic image was taken 2 hours after an invasion experiment at 8.5 MPa and 45 °C and a 1 M NaCl brine (Kim et al. 2012).

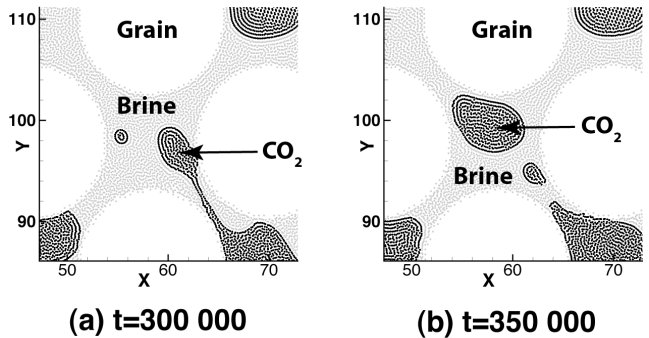
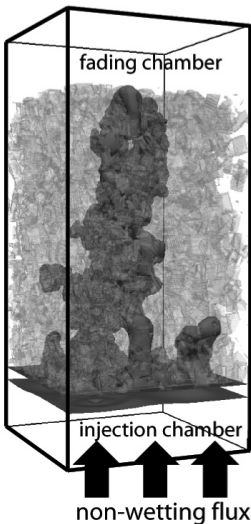


Figure 5. (a) Injection of non-wetting phase into a brine, leading eventually to capillary trapping once injection has ceased (Parmigiani et al. 2011) (b) Snap-off of a CO₂ bubble as capillary forces become dominant over gravitational or viscous forces (Bandara et al. 2011).

tension effects then need to be considered through the stress tensor in the Navier-Stokes equations. The Cahn-Hilliard diffuse interface model describes the free energy density (free energy per unit volume) of a binary two-component fluid or a single component fluid by a free energy functional (Cahn and Hilliard 1958). Further details of the Cahn-Hilliard model and its application in multiphase pore scale models may be found in de Gennes (1985), Meakin and Tartakovsky (2009), Xu et al. (2009), Bogdanov et al. (2011), and Parmigiani et al. (2011).

PHYSICS OF MULTICOMPONENT SOLUTE TRANSPORT AT THE PORE SCALE

Steefel and Maher (2009) provide a review of transport processes in porous media from the perspective of their role as driving force for many of the reactions in the water-rock interaction processes. In particular, transport processes are responsible for continuously introducing fluid out of equilibrium with respect to the reactive solid phase. Injection of CO₂ in the subsurface is an extreme case of this scenario. The review by Steefel and Maher (2009) emphasizes concepts applicable when the porous medium can be treated as a continuum in which a representative elementary volume (REV) is significantly larger than the average grain size. When considering the pore scale, however, phenomenological laws such as Darcy's law, the concept of tortuosity applied to diffusion or the Fickian treatment of mechanical dispersion are not necessary. These processes are captured naturally from a pore scale description of fluid flow and transport of chemical species because the detailed flow paths are explicitly considered. Understanding how these parameters are upscaled from the pore scale to the continuum scale is an active field of research. In this section, we introduce the fundamentals of transport at the pore scale and discuss how these pore scale transport processes relate to continuum scale parameters.

Advection

Advection involves the translation in space of dissolved or suspended material at the rate of movement of a bulk fluid phase. The advective flux, J_i^{adv} , of a dissolved species in the pore space of a porous medium can be described mathematically as

$$J_i^{adv} = \mathbf{u} \cdot c_i \quad (12)$$

where c_i is the concentration of the i^{th} species. The fluid velocity vector \mathbf{u} is calculated as a solution of the Navier-Stokes equations (Eqns. 6 and 7) or Stokes equation (Eqns. 9 and 7).

Diffusion

In contrast to advection, where mass transport involves the motion of a bulk fluid phase, diffusion results in mixing of the multicomponent mixture of solutes. Although it can also be derived atomistically (Lasaga 1998), Fick's First Law, which is applicable at the pore scale, provides a phenomenological theory for diffusion relating the diffusive flux to the "driving force" given by the concentration gradient:

$$J_i^{diff} = -D_i \nabla c_i \quad (13)$$

where D_i is the diffusion coefficient specific to the chemical component considered as indicated by the subscript i . In the more general case, a diffusive flux is driven by gradients in chemical potential

$$J_i^{diff} = -L_{ij} \nabla \mu_i \quad (14)$$

where μ_i is the chemical potential of the i^{th} species and the L_{ij} are the Onsager coefficients that couple the individual chemical components in the system (Steefel and Maher 2009). The more rigorous treatment of the chemical potential as providing the driving force for molecular diffusion implies that gradients in activity coefficients as well as concentration need to be considered.

Electrochemical migration

In the case of diffusion of charged species in dilute solutions, it is also necessary to consider an electrochemical migration term derived from the Nernst-Planck equation that is most commonly related to diffusion of charged species at different rates (Ben-Yaakov 1972; Lasaga 1979; Felmy and Weare 1991; Van Cappellen and Gaillard 1996; Giambalvo et al. 2002; Boudreau et al. 2004; Maher et al. 2006; Appelo and Wersin 2007; Li et al. 2008; Steefel and Maher 2009; Liu et al. 2011). Molins et al. (2012) showed that neglecting electrochemical migration in the single pore calcite dissolution experiment of Li et al. (2008) can introduce significant errors, especially under low-pH conditions. Ovaysi and Piri (2013) also observe that for weakly acidic conditions, electrostatic forces only affect transport slightly; however, when SO_2 and CO_2 are injected simultaneously, electrostatic forces significantly influence the solution composition in the pore space. More recently, Rolle et al. (2013) explored the effects of multicomponent diffusion on transverse dispersion/diffusion, an effect that could be important at the smaller length scales associated with the pore structure. Molecular diffusion and electrochemical migration are described by

$$J_i^{migr} = -z_i u_i F c_i \nabla \Phi \quad (15)$$

where z_i is the charge of the species, u_i is its mobility, F is Faraday's constant ($= 96,487$ Coulombs per mole of electrons), and Φ is the electrical potential. The mobility refers to the average velocity of a species in solution acted upon by a unit force, independent of the origin of the force.

Péclet number

The Péclet number, $Pe = (|u|l / D_i)$ is commonly used to evaluate the relative importance of advective and diffusive transport processes, where l is a characteristic length of the porous medium (at the pore scale, typically the average grain size). Even in the dynamic flow conditions induced by the CO_2 injection, a large portion of the reactivity of target storage formations may be located in low porosity and permeability material, where molecular diffusion is the dominant transport mechanism. So while the high permeability zones are disproportionately important for the consideration of flow, low permeability zones may be extremely important when reactive processes are considered. In addition, at the scale of a pore, even when advective transport dominates in the bulk solution far from the mineral surface, the no-slip condition at the mineral grain surface results in low fluid velocities in a thin boundary layer around the grains. In this region diffusive processes can be of significance, in particular insofar as this limits the mass flux to reactive surfaces. Well mixed conditions cannot be assumed in pores where gradients in concentrations lead to rate limiting conditions (Li et al. 2008). An example of flow and transverse diffusion in a cylindrical pore developed in calcite is shown in Figure 6. Note the development of a characteristic parabolic velocity profile associated with Poiseuille flow and the diffusion boundary layer adjacent to the no-slip reactive boundaries of the pore.

Damköhler numbers

The Damköhler numbers, Da_I and Da_{II} , are another set of important dimensionless parameters that are useful in the context of pore scale processes. They provide a comparison of the characteristic times for reaction (t_R) and advective (t_A) and diffusive (t_D) transport

$$Da_I = \frac{t_A}{t_R} = \frac{kl}{|u|} \quad (16)$$

$$Da_{II} = \frac{t_D}{t_R} = \frac{kl^2}{D} \quad (17)$$

where k is the reaction rate constant, l is again the length scale of interest (typically the grain

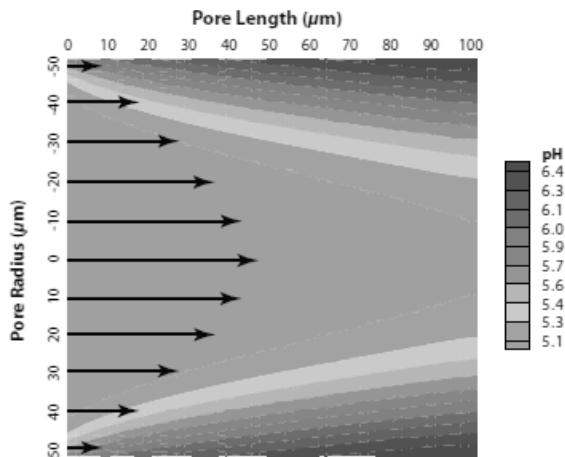


Figure 6. pH distribution in a single cylindrical pore developed in calcite (Li et al. 2008). The solution entering from the left is slightly acidic and therefore undersaturated with respect to calcite, which dissolves. Dissolution only occurs at the calcite-solution interface.

diameter at the pore scale), and D is the diffusion coefficient. Because of the variations in velocity at the pore scale (which are often not resolved at the larger continuum scale), the Da number in particular can be expected to vary significantly in space and time.

Upscaling of flow and transport processes to continuum scale parameters

Darcy flow and permeability. In a cylindrical core subject to a single phase flow through experiment, permeability in the flow direction can be calculated using the one-dimensional Darcy’s equation (e.g., Noiriél et al. 2004; Luquot and Gouze 2009):

$$k = \frac{\mu L}{S} \frac{Q}{\Delta P} \tag{18}$$

where L is the length of the sample in the flow direction, and S is the cross sectional area of the sample.

For two-phase CO_2 -brine flow at steady state, the relative permeability of the non-wetting phase at the inlet ($k_{r,nw}(\Delta P_{c,1})$) is proportional to the slope of the curve formed by the plot of the injection flow rate Q as a function of the steady-state pressure drop $\Delta P_{c,1} = \Delta P - P_{c,e}$ (Pini and Benson 2013):

$$\frac{dQ}{d\Delta P_{c,e}} = k_{r,nw}(\Delta P_{c,e}) \frac{Sk}{L\mu_{nw}} \tag{19}$$

where $P_{c,e}$ is the entry capillary pressure, i.e., the minimum pressure at which the permeability to the nonwetting phase takes a finite value.

Diffusion and tortuosity. Tortuosity is defined as the ratio of the path length the solute would follow in water alone, L_p , relative to the tortuous path length it would follow in porous media, L_e (Bear 1988) (see Fig. 7):

$$\tau = \left(\frac{L_p}{L_e} \right)^2 \tag{20}$$

In this definition, the value of the tortuosity is always < 1 and the effective diffusion coefficient in porous media is obtained by multiplying the tortuosity by the diffusion coefficient for the solute in pure water. With this formulation, the diffusion coefficient in porous media is given by

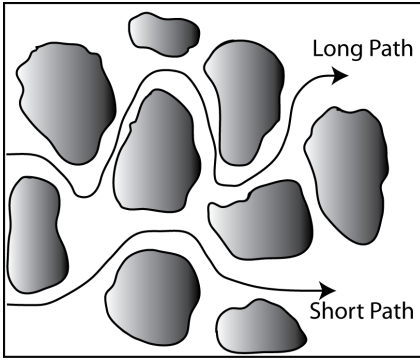


Figure 7. Tortuous diffusion paths in porous material, from Steefel and Maher (2009).

$$D_i^* = \tau D_i \tag{21}$$

At the pore scale, the effective diffusion coefficient D_i^* can be determined directly and thus used to calculate a tortuosity coefficient applicable at continuum scale. In a CO₂ experiment, Gouze and Luquot (2011) used segmented microtomographic images to calculate a tortuosity value with a random walk method based on the principles of Einstein (1956). The method involves computing the mean square displacement of a large ensemble of N_p particles at long time ($t \rightarrow \infty$):

$$D_i^* = \lim_{t \rightarrow \infty} \frac{\sum_{n=1}^{N_p} |\mathbf{x}_n(t) - \mathbf{x}_n(0)|^2}{N_p \cdot 6t} \tag{22}$$

where $\mathbf{x}_n(t)$ is the position of the n^{th} particle at time t .

Dispersion. As a result of the fact that variations in the velocities exist within the pore space, a non-reactive tracer released up gradient will not advance as a sharp front, but rather will appear as a disperse or gradual breakthrough at the down gradient end of the porous medium. This process, known as mechanical dispersion, was first clearly discussed for the case of laminar flow and transport within a cylindrical tube (Taylor 1953). A cylinder can be used for a first order description of an individual pore in which velocities adjacent to a solid grain are slower than the velocities in the center of the pore (Li et al. 2008). This effect is referred to as Taylor-Aris dispersion (Bear 1988; Steefel and Maher 2009), as in Figure 8.

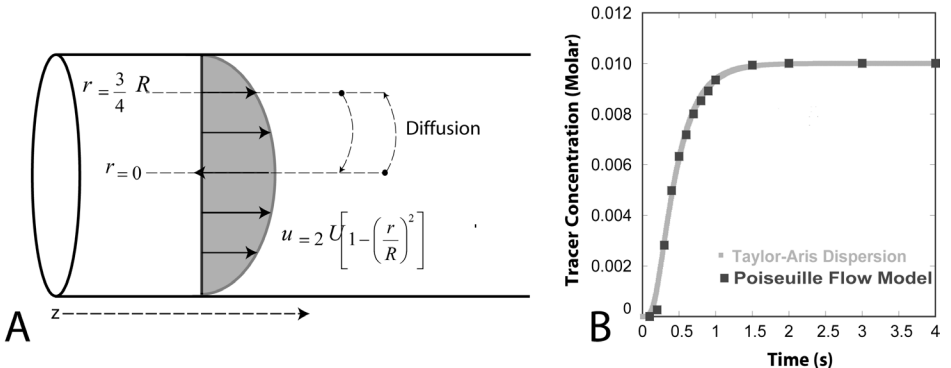


Figure 8. Taylor-Aris dispersion within a cylindrical pore (after Steefel and Maher 2009).

Additional effects in porous media are related to the tortuosity of flow paths and to differences in pore size, since velocities will be higher in those pores with wider apertures. When concentrations are resolved at the pore scale, the asymptotic longitudinal dispersion coefficient can be quantified using the second moment of the concentration of a non-reactive tracer (Le Borgne et al. 2011; Blunt et al. 2013; Varloteaux et al. 2013)

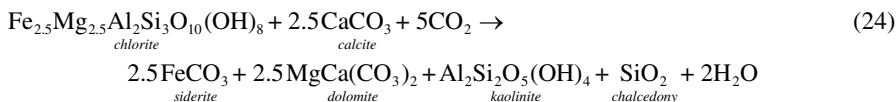
$$D_e = \frac{1}{2} \lim_{t \rightarrow \infty} \frac{d}{dt} \left\{ \frac{\int c(\mathbf{x}, t) x^2 d\mathbf{x}}{\int c(\mathbf{x}, t) d\mathbf{x}} - \left[\frac{\int c(\mathbf{x}, t) x d\mathbf{x}}{\int c(\mathbf{x}, t) d\mathbf{x}} \right]^2 \right\} \quad (23)$$

GEOCHEMICAL PROCESSES AT THE PORE SCALE

The various trapping mechanisms for CO₂ in the subsurface have been summarized by Gaus et al. (2008). The mechanisms involving geochemistry include 1) solubility trapping, in which the CO₂ gas or supercritical phase dissolves in the aqueous phase up to its solubility according to Equation (1), and 2) mineral trapping. The long term trapping of CO₂ in the subsurface is generally considered to involve carbonate precipitation. Capillary trapping can be influenced by chemistry through the mineralogical influence on interfacial free energy (see Tokunaga and Wan 2013, this volume), and is also important as an intermediate step between capillary and mineral trapping. In addition to carbonate precipitation reaction, other reactions that include precipitation of salt or silicate phases may play a role in modifying the pore structure of the subsurface and thus may need to be considered as well, even though they do not contribute to CO₂ sequestration.

Mineral dissolution is important as a cation source for carbonate precipitation, as well as serving as a source of alkalinity (and thus raising the pH) to decrease the solubility of the carbonate phases that can precipitate. In addition, dissolution can modify the pore structure, potentially increasing the porosity and permeability of the subsurface medium and/or fractures. In the case of the dissolution of carbonate minerals under the acidic conditions characterizing CO₂ injection and sequestration, wormholing or “reaction fingering” may occur (Steefel and Lasaga 1990; Steefel and Maher 2009; Carroll et al. 2013; Elkhoury et al. 2013). Precipitation of halite, clays, sulfate (gypsum), and carbonate phases can potentially result in clogging (Muller et al. 2009).

In general, the geochemical processes operating at the pore scale are the same as those investigated at the continuum scale, even if additional issues associated with pore scale transport and kinetics emerge (Steefel et al. 2005). Audigane et al. (2007) presented many of the relevant reactions for the Sleipner site in the North Sea, including the replacement of chlorite and calcite by siderite, dolomite, kaolinite, and chalcadony



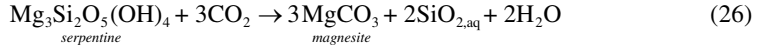
This represents an idealized stoichiometry that assumes perfect conservation of some of the components, an unlikely scenario when transport and kinetics are involved. Similar reactions may be written for the dissolution of the micas under high CO₂ conditions (mica and biotite), as well as the clay minerals kaolinite and illite. Another reaction much discussed in the literature involves the replacement of albite (Na-plagioclase) by dawsonite (Audigane et al. 2007)



where the reaction has been modified to produce aqueous silica rather than a specific silica

phase. As pointed out by Hellevang et al. (2011), this is potentially an important point, since many of the geochemical simulations that have predicted the formation of dawsonite did so because of the assumption of the formation of quartz, which is associated with a low silica activity in solution that favors dawsonite precipitation (see also Benezeth et al. 2007 for a discussion of the thermodynamics of dawsonite).

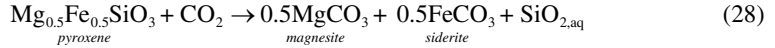
In more mafic rocks, reactions involving the formation of Fe and Mg carbonates become more important. For example, the dissolution of serpentine under high CO₂ conditions to form magnesite can be written as (e.g., Boschi et al. 2009)



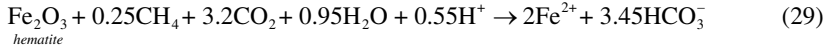
Olivine (written here as Fo₅₀, or 50% Mg and 50% Fe) present in basaltic or ultramafic rocks can react similarly with CO₂ (e.g., Daval et al. 2009)



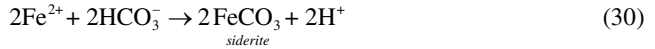
as can the mineral pyroxene



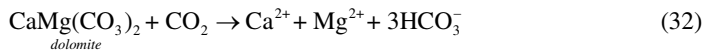
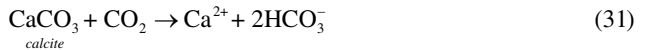
Other minerals than silicates may dissolve under high CO₂ conditions, as for example the Fe-oxyhydroxides described from the Green River Formation (Wigley et al. 2012)



leading potentially to the formation of siderite



In carbonate aquifers, the dissolution of carbonate phases calcite and dolomite may have a significant effect on aquifer porosity, permeability and pH, even if they do not contribute to net CO₂ sequestration



Mineral dissolution and precipitation reaction rates

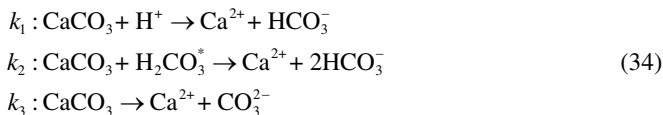
Bulk mineral reversible dissolution and precipitation reaction rates have been described by transition state theory (TST) (Lasaga 1981; Burch et al. 1993; Hellmann and Tisserand 2006) as the product of a far-from-equilibrium term and an affinity (or Gibbs Free Energy, ΔG) term that goes to zero at equilibrium

$$r_m = k_m \exp\left[-\frac{E_a}{RT}\right] \prod a_i^n \left[1 - \exp\left(m_2 \left(\frac{\Delta G}{RT}\right)^{m_3}\right)\right]^{m_1} \quad (33)$$

where k_m is the intrinsic rate constant (mol m⁻² mineral s⁻¹), E_a is the activation energy (kcal mol⁻¹), $\prod a_i^n$ is a product representing the inhibition or catalysis of the reaction by various ions in solution raised to the power n , ΔG is the Gibbs free energy (kcal) with m_1 , m_2 and m_3 being three parameters that affect the affinity dependence, R is the ideal gas constant, and T is the temperature. In the case of far from equilibrium dissolution, the affinity or ΔG term can often be neglected, as in the studies of chlorite dissolution under high pCO₂ conditions (Smith et

al. 2013a), although care must be taken to ensure that this can be justified, particularly in the case of the silicate minerals where there may be a dependence of the rates over a very broad range of ΔG values (Burch et al. 1993; Hellmann and Tisserand 2006). For application to CO_2 injection and sequestration problems, the parameters in Equation (33) need to be determined under the relevant conditions, e.g., high salinity and high pCO_2 (Pokrovsky et al. 2009; Smith et al. 2013a,b).

For modeling of carbonate dissolution at the pore scale, Molins et al. (2012) used the rate laws proposed and parameterized by Plummer et al. (1978) and Chou et al. (1989):



The rate of calcite dissolution is described by the transition state theory as the product of a far-from-equilibrium term and an affinity (or ΔG) term that goes to zero at equilibrium

$$r_{\text{CaCO}_3} [\text{mol m}^{-2} \text{mineral s}^{-1}] = \left(k_1 a_{\text{H}^+} + k_2 a_{\text{H}_2\text{CO}_3^*} + k_3 \right) \left(1 - \frac{a_{\text{Ca}^{2+}} a_{\text{CO}_3^{2-}}}{K_{eq}} \right) \quad (35)$$

where k_1 , k_2 and k_3 are the rate constants [$\text{mol m}^{-2} \text{mineral s}^{-1}$]; K_{eq} is the equilibrium constant of the reaction; and a_{H^+} , $a_{\text{H}_2\text{CO}_3^*}$, $a_{\text{CO}_3^{2-}}$, and $a_{\text{Ca}^{2+}}$ are the activities of H^+ , H_2CO_3^* , CO_3^{2-} , and Ca^{2+} [dimensionless] respectively. At 25 °C, $k_1 = 0.89$, $k_2 = 5.01 \times 10^{-4}$, $k_3 = 6.6 \times 10^{-7} \text{ mol m}^{-2} \text{ s}^{-1}$ (Chou et al. 1989), and $\log K_{eq} = -8.234$ (Wolery et al. 1990). The pCO_2 dependent parameter provided by Chou et al. (1989) is not adequate to describe rates at higher pCO_2 values and the data given by (Pokrovsky et al. 2009) should be used instead.

More recently, the applicability of the TST rate formulations have been called into question on several levels. One issue has to do with the reversibility implied in the TST formulation(s), since it appears that for most (or all) of the silicates and even carbonate phases, precipitation and dissolution cannot be described with the same rate law and set of parameters (Yang and Steeffel 2008; Hellevang et al. 2011; Saldi et al. 2012). For both dissolution and precipitation, multiple rate laws may need to be used in order to capture the behavior over the entire range of ΔG . For dissolution, there may be a transition from nearly linear dissolution close to equilibrium to a more nonlinear dependence on ΔG farther from equilibrium as etch pit formation and propagation become more important (Burch et al. 1993). For precipitation, the situation is even more complicated, with transitions from spiral growth to 2D surface nucleation occurring as the supersaturation increases (Teng et al. 2000; De Yoreo and Vekilov 2003; Noiriél et al. 2012).

A more fundamental issue has to do with the lack of an atomistic treatment of mineral dissolution and precipitation. Atomistic treatments of mineral dissolution and precipitation demonstrate clearly the limitations of the bulk TST approaches (e.g., Teng et al. 2000; Nielsen et al. 2012; Wolthers et al. 2012). For example, a simple TST rate law like that given in Equation (33) or in Equation (35) fails to capture the dependence of the rate on the calcium to carbonate activity ratio (Nehrke et al. 2007; Gebrehiwet et al. 2012; Nielsen et al. 2012; Wolthers et al. 2012; Bracco et al. 2013). Perhaps even more telling is the inability of the simpler forms of the TST to capture kinetic isotopic fractionation adequately (Nielsen et al. 2012; Druhan et al. 2013). Certainly a more atomistic treatment of dissolution and precipitation is required as the interest increases in developing mesoscale models for mineral reactions at the pore scale (Bracco et al. 2013).

The major obstacle to the use of the atomistic models is the lack of a dynamic description of time-dependent mineral surface reactivity. The types and density of specific reactive

sites on the mineral surface is poorly constrained by the theoretical models, and numerical techniques like Kinetic Monte Carlo have not yet been routinely developed that can capture the thermodynamic and kinetic controls associated with multicomponent solution chemistry. In fact, one is hard pressed to find an adequate reconciliation of site densities and bulk reactive surface area, despite the importance of this topic and the large amount of work being carried out on atomistic crystal growth and dissolution rates. Arguably, the first successful example of this reconciliation has been provided by Bracco et al. (2013). Thus, additional work needs to be done to implement fully dynamic atomistic mineral dissolution and precipitation rate laws in the modeling tools that can be used to describe pore scale CO₂ injection and sequestration at the meso to macroscale.

Another issue has to do with the potential rate limitation associated with transport to and from the mineral surface, a topic that has been relatively neglected in the geochemical literature in recent years. When the transport of reactants to the reactive surface is very fast, the dissolution or precipitation reaction rate is controlled by the kinetic barrier, i.e., the rate of attachment and detachment of ions from the mineral surface. However, in general, transport processes will exert some control on the overall reaction rates, particularly when interface reaction rates are high. This effect is potentially most important in the case of calcium carbonate, which shows a partial diffusion rate control in rotating disk experiments even at 25 °C and circumneutral pH (Pokrovsky et al. 2005; Noiriel et al. 2012). It is generally agreed that calcite dissolution is completely transport controlled at pH values below 4—at higher pH values, calcite dissolution shows a mixed control, which is more difficult to treat in larger scale, continuum models (Noiriel et al. 2012). If a sufficiently high spatial resolution (order micron scale) is available at the pore scale, however, the interplay between molecular diffusion and surface reaction may be captured naturally (Molins et al. 2012; Yoon et al. 2012; Hiorth et al. 2013). When the reaction is assumed to take place at the mineral-fluid interface, the mass flux \mathbf{J} perpendicular to the surface for mineral precipitation-dissolution reaction must be equal to reaction rate \bar{r} expressed per unit of physical interfacial area (mol m⁻² s⁻¹)

$$\mathbf{J} \cdot \mathbf{n} = \bar{r} \quad (36)$$

where \mathbf{n} is a unit vector normal to the interface. Figure 9 shows an example 2D calculation of flow, diffusion, and reaction around a calcite crystal using the Chombo-Crunch pore scale modeling software (Molins et al. 2012) and the rate laws given in Equation (35) at 25 °C and pH 7.5 to 9 (injection solution is pH 7.5). The presence of concentration gradients, which are most pronounced for larger grain sizes (> 200 microns), indicates a partial diffusion control of the dissolution rate. A square geometry for the calcite grain was assumed so as to avoid grid orientation effects, although the verification subsequently indicated that this was not necessary for Chombo-Crunch.

PORE SCALE CHARACTERIZATION AND EXPERIMENTATION

A number of new pore scale experimental and characterization approaches have emerged or matured in recent years that have made it possible, along with the new modeling approaches (see below), to investigate the physical and chemical processes associated with CO₂ injection and sequestration with unprecedented spatial resolution and process fidelity. These methods include 2D backscattered electron mapping (BSE), 3D microtomography based on X-ray computed microtomography diffraction (XMCT) and focused ion beam-scanning electron microscopy (FIB-SEM), small angle neutron scattering (SANS), nuclear magnetic resonance (NMR), and 2D micromodels. On the experimental side, there is great potential for progress in understanding CO₂ injection and sequestration processes with the use of engineered microfluidic and nanofluidic devices that simulate natural pores, although we are only just beginning to see applications in this field (Yoon et al. 2012).

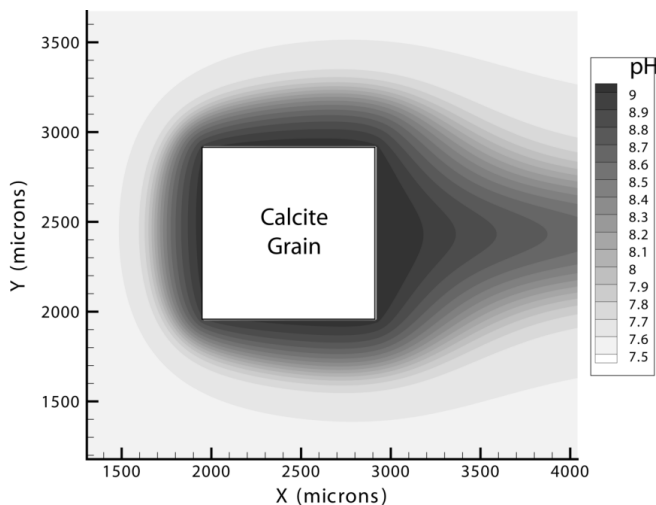


Figure 9. Diffusion boundary layer in solution pH developed around a dissolving calcite grain in two dimensions, the flow field of which is shown in Figure 3. The simulation was carried out with the software Chombo-Crunch (Molins et al. 2012) and verified against simulations using CrunchFlow with a velocity field imported from Chombo.

2D backscattered electron mapping

Backscattered electron microscopy is a powerful technique for mapping porosity and mineral distributions at the pore scale, as first demonstrated by Peters (2009) in her analysis of CO₂ reservoir sandstones from the Alberta Basin in Canada. The technique is based on the use of scanning electron microscopy (SEM) operated in backscatter mode to produce elemental maps that, when combined with the appropriate thresholding technique, can be used to produce mineral distribution maps. The approach is generally supplemented by local or point X-ray dispersive (EDX) analysis for semi-quantitative or quantitative (when combined with standards) determination of mineral chemistry. The technique is particularly powerful in that it can be combined with mapping of porosity (both connected and unconnected) so as to quantify the hydrologically accessible reactive surface area (Peters 2009; Landrot et al. 2012). Since the approach is based on surface backscattering, it is usually treated as a 2D technique, although if combined with FIB-SEM, in which successive layers of the solid material are destructively interrogated, it can be made fully 3D.

Peters (2009) investigated the Viking sandstone in the Alberta sedimentary basin in Canada and found that porosities ranged from 20% to as low as 8%. Based on their thresholding analysis, they were able to map kaolinite as the dominant secondary mineral phase in the sediment ranging from 5% to 31% of the mineral content on a volume basis. However, Peters (2009) also found that kaolinite comprised 65% to 86% of the pore-mineral contacts based on the mapping, indicating that it accounted for most of the reactive surface area in the sediment. On this basis, Peters (2009) determined that reactive surface area (RSA) could be overestimated by as much as 3 to 5 times if mineral volume fractions alone were used as the basis for the estimate (i.e., by simply multiplying the concentration of the mineral by its specific surface area).

Similar conclusions were reached by Landrot et al. (2012), who investigated the accessible RSA of a reservoir sand from the Cranfield Formation in Mississippi. Landrot et al. (2012) employed a hybrid approach in which 2D BSE mapping supplemented by EDX chemical

analysis with resolution as high as 330 nm was combined with 3D X-ray microtomography at a resolution of 880 nm (Fig. 10). Scale-dependent correction factors for the porosity and mineral distributions were obtained by carrying out the BSE mapping at both the higher resolution of 330 nm and at the 880 nm resolution of the X-ray microtomography (Landrot et al. 2012). Locally, they also collected FIB-SEM data at a 14 nm resolution to map chlorite-filled pores.

Anovitz et al. (2013) used BSE on samples of the St. Peter Sandstone to extend their Ultra Small Angle Neutron Scattering (USANS) and Small Angle Neutron Scattering (SANS) results to larger scales (see below).

3D microtomography (XCMT and FIB-SEM)

Ideally, the pore structure of a sediment or rock intended as part of a CO₂ reservoir or a caprock intended to prevent its buoyant rise should be mapped in three dimensions. The X-ray CT technique involves an X-ray source, an object, and a detector. The source generates X-rays that are directed toward an object that is rotated in a stepwise manner. The X-rays are attenuated as they pass through the object and the emerging or transmitted X-ray intensity is measured and recorded by the detector for every step of rotation. The data is typically collected as a series of 2D radiographs that are then stacked together to provide spatially resolved 3D images. The attenuation of X-rays by an object may be modeled using Beer's law, which is valid for monochromatic radiation passing through homogeneous materials. Nanometer scale resolution is achievable in some cases, but only with a tradeoff in the volume of material that can be investigated. Synchrotron-based X-ray sources like those at the Advanced Photon Source (Argonne National Laboratory) and the Advanced Light Source (Lawrence Berkeley National Labora-

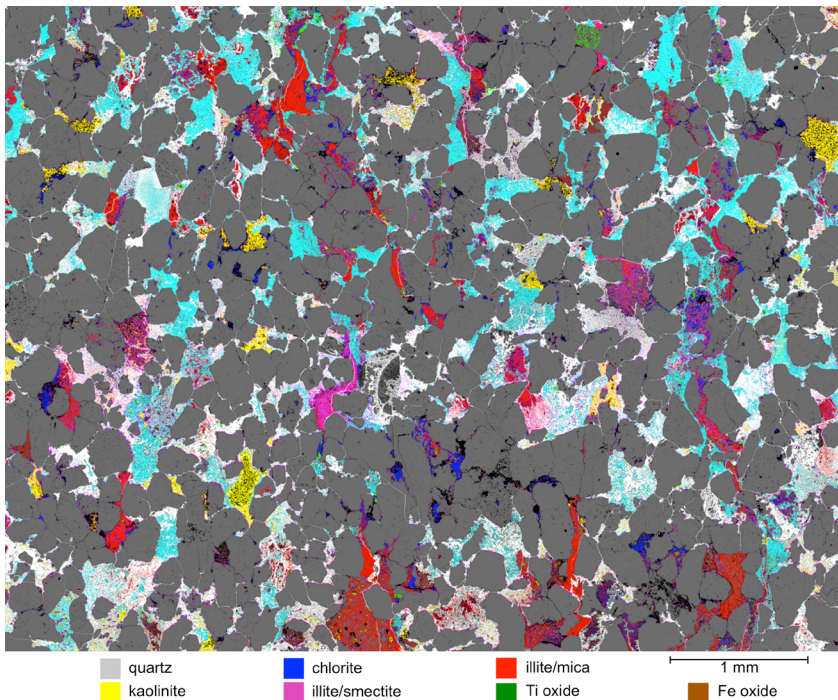


Figure 10. BSE map of reactive phases and porosity in a 2D sample from the Cranfield Formation in Mississippi, a CO₂ injection test site (Landrot et al. 2012). Connected porosity is uncolored. Both shades of blue represent chlorite, with the lighter blue made up of nanoporous chlorite.

tory) provide higher energy than is achievable typically with commercially available units.

X-ray based microtomography (μ CT or XCMT) techniques have been used in a number of studies of the physics and chemistry of CO_2 injection and sequestration. Noiriel et al. (2004, 2009) used periodic X-ray microtomographic analysis at a resolution of $4.91 \mu\text{m}$ to map local changes in porosity, pore roughness, and reactive surface area in a limestone subjected to CO_2 -acidified water. In the case where a single mineral is present and dissolving, the increase in porosity also represents the net amount of the mineral dissolved. Estimates based on the volume of mineral lost can be compared to the estimate of total dissolution over the length of the sample determined from effluent chemistry (e.g., based on the flux of calcium). Similarly, Luquot and Gouze (2009) and Gouze and Luquot (2011) used the technique to map dissolution of carbonate as a function of time, demonstrating that slower flow conditions (corresponding to high Damköhler numbers) resulted in “wormholing” or reaction fingering (Ortoleva et al. 1987; Hoefner and Fogler 1988; Steefel and Lasaga 1990). Smith et al. (2013a) used the approach to contrast dissolution rates and pore geometry evolution in an evaporite caprock. Carroll et al. (2013) extended the analysis to two contrasting rock types, a vuggy limestone (which showed extensive wormholing) and a marly dolostone (which did not), both from the Weyburn CO_2 injection site in Alberta, Canada (Fig. 11). They also took the novel next step of using the microtomography data to provide conditions to initialize a 3D reactive transport model, the results from which were then compared to post-experiment microtomographic maps of the same rock. Although not a true pore scale analysis, based as it was on a continuum representation of a porosity-permeability relationship, it made use of micron scale resolution data of the evolving porosity structure of the rock.

Noiriel et al. (2012) carried out a combined XMCT and chemical analysis of carbonate precipitation as a result of mixing. The experimental scenario was intended to represent the processes likely to occur when the CO_2 -rich acidic brine is neutralized and mixed with a source of calcium ions. As in the case of limestone dissolution, calcite was determined to be the only phase to form, so the porosity decrease determined at a 4.4 micron resolution could be treated as local precipitation of calcite. The addition of carbonate precipitate after 28 days of reaction is clearly visible in the reconstructed images from the XCMT analysis (Noiriel et al. 2012) (Fig. 12). The study demonstrated that the rates of local (micron scale) reaction could be reconciled with independently determined reaction calcite precipitation rates in the absence of transport or “porous medium” effects (Noiriel et al. 2012).

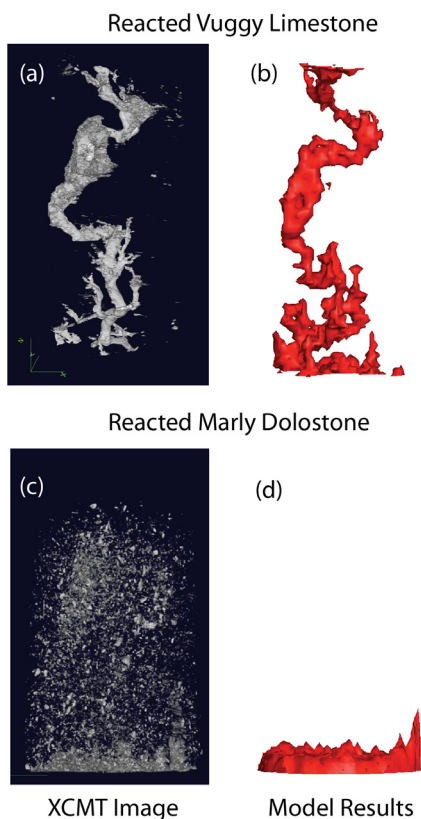


Figure 11. XCMT images of dissolution features in a) a vuggy limestone, and c) a marly dolostone from the Weyburn Formation CO_2 injection site in Alberta, Canada. Panels (b) and (d) on the right represent model results that made use of the initial porosity distribution and an assumed porosity-permeability relationship (Carroll et al. 2013).

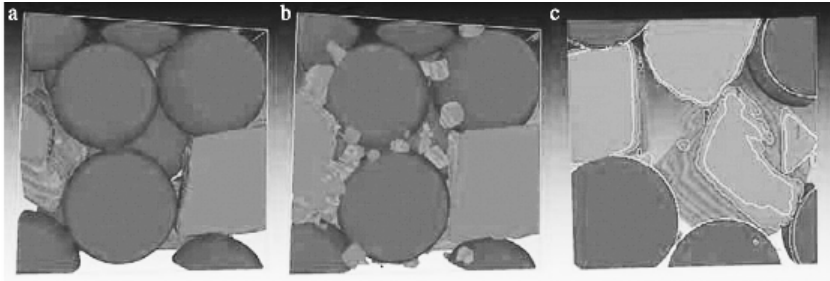


Figure 12. Carbonate precipitation on glass beads (dark gray spheres) and calcite spar (medium gray rhombic crystals) before reaction (Panel A) and after 28 days of reaction with a flowing supersaturated solution (Panel B) Panel C shows the displacement of the crystal-solution interface (pale lines) as a result of precipitation. From Noiriél et al., 2012.

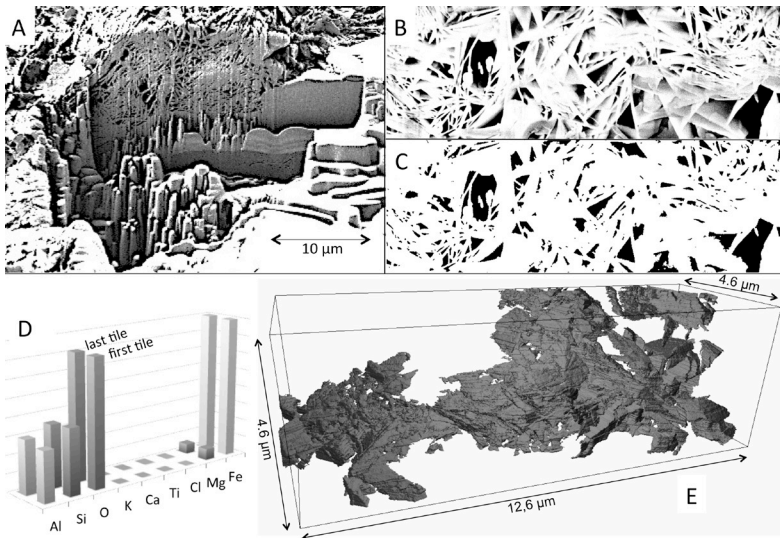


Figure 13. FIB-SEM microtomography of chlorite from a pore in the reservoir sandstone from the Cranfield, Mississippi scCO_2 injection site (Landrot et al. 2012). A) Excavated portion of the chlorite-filled pore, with a quartz grain on the right. B and C) SEM close up of chlorite showing nanoporosity. D) EDX results showing Fe-chlorite composition. E) Microtomographic image of chlorite-filled pore.

Focused Ion Beam-Scanning Electron Microscopy (FIB-SEM) was used to provide 3D microtomographic data at scales below the resolution of the XCMT techniques (Landrot et al. 2012) (Fig. 13). FIB-SEM is a destructive technique that gradually excavates new 2D layers, which are then imaged with the SEM (supplemented by EDX analysis, if available). The technique provides data that can be interpreted in a similar fashion to the XCMT, with counting of voxels to establish porosity and the use of a burning algorithm to determine connected porosity (Landrot et al. 2012). Landrot et al. (2012) applied the technique to chlorite filled pores in a reservoir sandstone from the Cranfield Formation in Mississippi at a resolution of 14.2 nanometers. Landrot et al. (2012) were able to determine that essentially all of the porosity (or nanoporosity) within the chlorite was connected. FIB-SEM was also used for the quantitative analysis of nanopore structures in a Cretaceous chalk sample (Yoon and Dewers 2013), revealing a nano-scale basis for strong anisotropy in the presence of fractures.

Multiphase studies of CO₂ injection and/or sequestration have been fewer, in part because of the difficulty in capturing the highly transient injection stage with time-consuming X-ray microtomographic techniques. Silin et al. (2011) and Blunt et al. (2013) used XCMT to image the two-phase fluid resolution resulting from CO₂ invasion of the Frio sandstone and the Doddington sandstone, respectively. Kneafsey et al. (2013) carried out a core-scale experiment in which supercritical carbon dioxide (scCO₂) was flowed through a brine-saturated sample consisting of a layer of silica sand, a layer of calcite sand, and then another layer of silica sand. The results were compared with an otherwise identical experiment in which nitrogen was the invading gas. Both experiments were carried out at 46.7 °C and 8.28 MPa. Panel A of Figure 14 shows the XCMT data before injection of the gases, with the contrast between the silica (dark grey, or purple in the original reference) and the calcite (light grey, or yellow in the original reference) clearly visible as a result of their density difference (Kneafsey et al. 2013). The upper left circular slice (3 mm thick) is closest to the injection port, while the lower right circular slice is furthest downstream. Panels B and C of Figure 14 show the distribution of nitrogen and scCO₂, respectively. Both gases show a buoyant rise to the top of the core after about 4 to 5 slices, flow through a very narrow pathway along the top of the core within the calcite sand, while taking a slightly broader pathway through the silica sand downstream. Presumably this difference in behavior reflects the difference in wetting behavior of the two non-aqueous fluids.

Pini and Benson (2013) presented a novel method to measure drainage capillary pressure curves both at the core and sub-core scale using CO₂ and water at reservoir conditions. Capillary pressure measurements were made at the inlet face of the sample by successively increasing the flow rate of the non-wetting phase while measuring the saturation with a medical X-ray Computed Tomography (CT) scanner. They found excellent agreement between the new method and data from mercury intrusion porosimetry, while also allowing for an estimate of the wetting and interfacial properties of the CO₂/water system.

Bauer et al. (2012) calculated macro and microporosity values for three carbonate rock samples (assumed monomineralic) by applying two thresholds to the distribution of measured intensities. These values were in close agreement with those measured from mercury intrusion.

Small Angle Neutron Scattering

Small Angle Neutron Scattering (SANS) and Ultra Small Neutron Scattering (USANS) are powerful techniques that make it possible to investigate a large range of pore sizes, although they are statistical rather than tomographic techniques (pore shapes are not directly imaged, but must be reconstructed on the basis of a geometric model). Nonetheless, their ability to extend analysis to nanometer sized pores makes them the methods of choice for investigating water-rock and CO₂-water-rock interaction as a function of pore size, particularly when nanoporosity is of interest. Anovitz et al. (2013) recently studied samples of St. Peter Sandstone that contain significant volumes of large-scale porosity, modified by quartz overgrowths, along with significant sub-micron porosity based on the neutron scattering results. In their study, autocorrelation data from BSE was used to extend the neutron scattering range (~1 nm to 10 μm) to investigate structures up to 1 cm. While data from sandstones collected previously suggested scattering is dominated by surface fractal behavior over many orders of magnitude, careful analysis of the St. Peters Sandstone data showed both fractal (high Q values in Fig. 15b) and pseudo-fractal behavior. The scattering curves are composed of subtle steps that can be modeled as polydispersed assemblages of pores with log-normal distributions (Fig. 15b).

Nuclear Magnetic Resonance (NMR) and Magnetic Resonance Imaging (MRI)

Nuclear Magnetic Resonance (NMR) and Magnetic Resonance Imaging (MRI) are additional techniques for directly imaging CO₂ injection at the pore scale. Suekane et al. (2005) used a magnetic resonance imaging (MRI) technique to directly visualize the distribution of supercritical CO₂ injected into a packed bed of glass beads containing water. After the CO₂

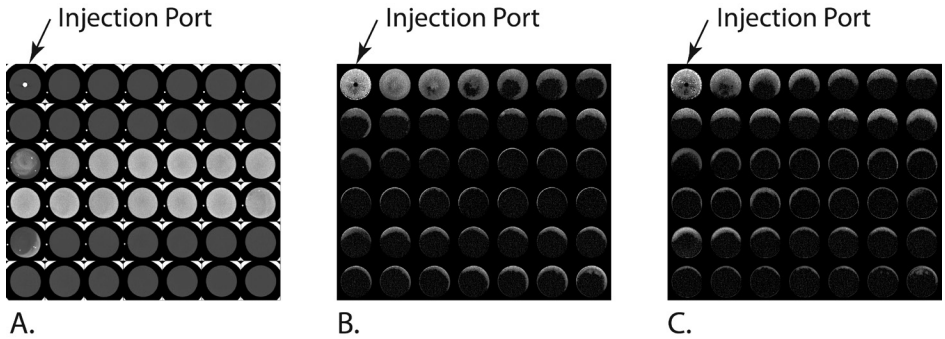


Figure 14. XCOM images of A) the pre-experiment silica (dark grey, or purple in the original reference) and calcite (light grey, or yellow in the original reference) sand distribution, clearly visible from the density contrast between the two minerals, B) the distribution of nitrogen, and C) the distribution of scCO_2 . The experiment was carried out at 46.7 °C and 8.28 MPa (Kneafsey et al. 2013).

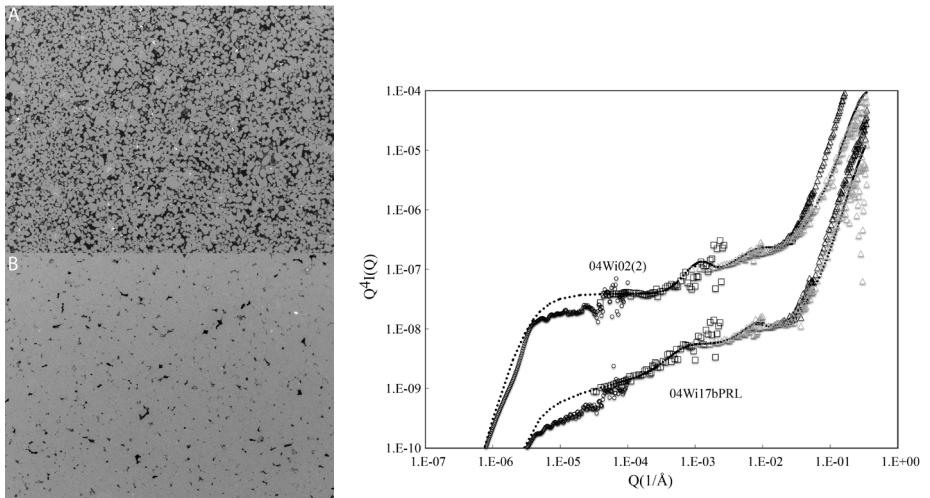


Figure 15. (a) SEM/BSE images of two samples from the St. Peter Sandstone (Anovitz et al. 2013) (b) Porod transform of the scattering curve for these samples (USANS data in boxes, SANS data in circles, BSE data in dashed lines). The lines show the log-normal, monodispersed sphere and form factor fits to the datasets (Anovitz et al. 2013).

displaced much of the water, some water remained near the central axis, although there were several millimeter-sized, CO_2 -rich channels running through this water-rich region. In a parallel channel with hydrophilic surfaces, a high velocity of water between the bubbles along the flow direction results in a high relative permeability at low water saturations. At high CO_2 saturations, a stable layer flow occurred, indicating that the relative permeability of water decreased sharply with saturation decreasing. In Suekane et al. (2009) a noninvasive nuclear magnetic resonance (NMR) technique was presented to measure the amount of CO_2 dissolved in water in porous rock. The relaxation time of the NMR signal was evidently shortened by the porous material surfaces and CO_2 dissolution. Hussain et al. (2011) used NMR techniques to quantify the spatial distribution and pore environment associated with CO_2 capillary trapping in a model porous medium (random glass bead packing). 3D images revealed relatively homogeneous (at

the macroscopic scale) CO₂ entrapment, even though the image resolution was insufficient to resolve individual CO₂ ganglia. Quantification of the pore environment of the CO₂ ganglia was achieved using NMR displacement propagators (displacement probability distributions), acquired both before and after CO₂ entrapment.

Micromodels

Micromodels are transparent pore networks used for laboratory studies of microscopic distribution and transport of fluids in porous media, with application to research related to oil recovery from reservoirs, nonaqueous phase liquid dissolution, and colloid transport (see also Crawshaw and Boek 2013, this volume). Micromodels have also been applied in reactive systems (e.g., Yoon et al. 2012). Few micromodel experiments have been conducted under elevated pressure and temperature, and even fewer have been conducted under supercritical scCO₂ conditions. Chalbaud et al. (2009) investigated distributions of CO₂ and water in glass micromodels having different wettabilities. Er et al. (2010) investigated the behavior of CO₂ and oil in homogeneous and heterogeneous fractured micromodels. Micromodel studies have been used to identify the crossover conditions from viscous to capillary fingering during invasion of liquid and supercritical CO₂, in heterogeneous and heterogeneous pore networks (Zhang et al. 2011; Wang et al. 2013). Discussion of the emergent features of associated with CO₂ invasion is provided below.

Kim et al. (2012) studied pore-scale wettability and wettability alteration in scCO₂-silica-brine systems using engineered micromodels at 8.5 MPa and 45 °C over a wide range of NaCl concentrations up to 5.0 M (Fig. 4). Dewetting of silica surfaces upon reactions with scCO₂ was observed through water film thinning, water droplet formation, and contact angle increases within single pores. The brine contact angles increased from initial values near 0° up to 80° with larger increases under higher ionic strength conditions. Given the abundance of silica surfaces in reservoirs and caprocks, these results indicate that CO₂-induced dewetting may have important consequences on CO₂ sequestration, including the reduction of capillary entry pressure, as well as the modification of CO₂ residual trapping, relative permeability, and caprock integrity.

INCORPORATING MICROSCOPIC CHARACTERIZATION INTO NUMERICAL PORE SCALE MODELS

Significant advancements in imaging techniques and processing capabilities have made it possible to resolve the porous media at micrometer scale. To incorporate these data into numerical models, images captured experimentally by microtomography need to be converted into input data for numerical models. Wildenschild and Sheppard (2013) have provided a comprehensive review of the approaches that can be used to segment images to obtain the morphology and topology of the pore space, the porosity, fluid saturation and spatial distribution, and the interface curvature estimation.

Segmentation is used to identify the discrete materials in an image, frequently by binarization of an image into just two materials, e.g., pore and solid. Noiriel et al. (2009) presented an approach to segmenting the images collected from X-ray microtomographic analysis of cores. They used a segmentation technique based on region growing (Gonzalez and Woods 2008) to avoid the errors associated with simple thresholding. Before the segmentation procedure, the data sets were normalized through a linear interpolation procedure to achieve consistency within a dynamic range of intensity values on the different images. The noise was reduced by running a 3D median filter. Then, the different parameters for segmentation were chosen by visual inspection of the grey-level histogram, and the results were validated by comparison of the segmented volumes with the greyscale ones. In the fitting procedure, the parameters used were forced to be the same for all of the sample intervals investigating. In the study by Noiriel

et al. (2012), a similar approach was taken, although in this case simple thresholding would have been sufficient because of the strong contrast between the two materials, glass beads and calcite spar. Armstrong and Ajo-Franklin (2011) also found that after applying a median filter ($3 \times 3 \times 3$ kernel), it was possible to use a simple threshold to segment the solid (glass and calcium carbonate) and liquid phases.

Following the segmentation procedure, the porosity of the sample can be evaluated. The next step consists in determining the percolation clusters, or sample spanning clusters, which are the networks of pores connected to the boundaries of the sample, and the unconnected pores using a cluster-labeling algorithm (Stauffer et al. 1994). A similar burning algorithm was employed by Landrot et al. (2012).

Beyond the morphology and topology of the pore space, geometric methods such the Method of Inscribed Spheres (MIS) can provide insights into two-phase fluid distributions in porous media (Silin and Patzek 2006). The method of MIS models these distributions from segmented micron-scale 3D images of natural rock assuming equilibrium dominated by the capillary forces (Silin et al. 2011). Kneafsey et al. (2013) computed characteristic curves for an experimental core of silica and calcite sand layers for a range of contact angles using the method of maximal inscribed spheres. Simple physical arguments and analysis using MIS indicated that CO_2 was wetting the calcite under the experimental conditions and duration of the experiment.

Most recently, Yoon and Dewers (2013) extended combination of image analysis and pore-scale modeling to 3D nanopore structures, suggesting the multiscale reconstruction was possible by mapping FIB-SEM data onto microCT dataset. Blunt et al. (2013) also described the underlying technology, namely imaging of the pore space of rocks from the nanometer scale upwards, coupled with a suite of different numerical techniques for simulating single and multiphase flow and transport through these images.

MODELING APPROACHES FOR THE PORE SCALE

Simulation of flow in the subsurface has historically relied on the treatment of the porous medium as a continuum in which a representative volume or REV is defined (Bear 1988). Within the REV at each point in space, all phases are assumed to exist simultaneously. At the pore scale, however, each point of space is occupied by a discrete phase (CO_2 or brine or solid). This requires incorporating directly the spatial distribution of the fluid and solid phases and their evolution with time. The initial phase distribution in actual rock or sediment samples is available from experimental characterization techniques as outlined in the previous section. Often for convenience and simplicity, especially for model validation or for testing of fundamental concepts, many modeling efforts are performed on synthetically generated domains where mineral grains are represented by spheres or other basic geometric shapes, rather than using actual porous media (Chen and Zhang 2010; Bandara et al. 2011). Sometimes these basic geometries correspond to those etched in experimental micromodels (e.g., Jung and Wan 2012; Yoon et al. 2012). Stochastic porous medium structures have also been generated by computer simulation (Sadhukhan et al. 2012) assuming a fractal pore-grain interface distribution (Dutta and Tarafdar 2003).

Recent literature reviews of pore scale models (Meakin and Tartakovsky 2009; Joekar-Niasar and Hassanzadeh 2012) reveal a large number of pore scale modeling studies of significance in problems ranging from hydrocarbons reservoir processes, vadose zone contamination or water-rock interaction, but only a limited number of works are devoted to CO_2 sequestration scenarios (Table 1). The availability of pore scale simulation methods and the recent interest in the subject suggest that the next few years will likely see a remarkable increase in pore scale models applied specifically to CO_2 sequestration problems.

Table 1. Selected list of published pore scale models relevant to CO₂ sequestration

Reference	Model	Sample	Approach	Resolution	Domain size
Ovaysi and Piri (2013)	sF-T	Berea and Bentheimer sandstones	MMPS particle method	5.345 μm	0.51×0.51×1.09 mm
Chen and Zhang (2010)	mF	Square grains and fracture in 2D	Lattice Boltzmann	25 μm	0.01×0.01 m
Flukiger and Bernard (2009)	sF-T-R	Packed spheres obtained from XCMT	Direct Numerical Simulation	10 μm	0.5×0.5×1.5 mm
Varloteaux et al. (2013)	T-R	Fontainebleau sandstone	Pore Network	80 μm	18.4 mm ³ &
Sadhukhan et al. (2012)	sF-T-R	2D stochastic	Finite difference, random walk method		128×1000 (unreported units)
Molins et al. (2012)	sF-T-R	Packed virtual spheres	Pore Network	7.8 μm	1.0 cm length, 0.5 cm diameter
Molins et al. (2012)	sF-T-R	Crushed calcite grains in capillary tube	Direct Numerical Simulation	1.1 μm	0.7 cm length, 0.5 mm in diameter
Yoon et al. (2012)	sF-T-R	Cylindrical grains from micromodel	Hybrid lattice Boltzmann and DNS	5 μm	2 cm length, 1 cm in width
Kang et al. (2007)	sF-T-R	2D Synthetic porous medium	Lattice Boltzmann	117 μm 125 μm	0.75×0.75 cm 5×0.75 cm
Blunt et al. (2013)	mF-T	Estailades carbonate, Ketton limestone, Mount Gambier carbonate	Pore Network	36-91 μm * &	18.7-31.3 mm ³
Ellis and Bazylak (2013)	mF	Rectangular lattice	Pore Network	3.2±1.5 μm	0.09×0.09×0.24 mm # &
Kim et al. (2011)	sF-T-R	Sandstones, Viking formation	Pore Network	67 μm * &	2.9×2.9×1.4 mm

NOTES:

sF = single fluid

mF = multiple fluid phases

T = transport

R = reactions

= estimated assuming cubic pores

= estimated assuming a porosity of 0.14

& = estimated assuming pore bodies make up entire pore space

Here we review the generic pore scale modeling approaches specifically as they can be or have been applied to modeling CO₂ sequestration scenarios. To address these scenarios, pore scale models need to resolve the relevant physical and chemical processes in complex pore geometries with interfaces between CO₂ and brine. This requirement demands very fine model resolution (on the order of a few microns) so that the physics and chemistry are accurately captured. However, the ultimate interest of many modeling applications is to be able to draw conclusions that are applicable over a representative volume of porous medium. For this purpose, large simulation domains are required. The two broad categories of approaches used to simulate pore scale processes are those that extract the pore space geometry to construct a pore network and those that consider the actual pore space geometry directly. Pore network models sacrifice the resolution of the complex pore space geometry of most rocks and soils by replacing it with a network of pore volumes connected by channels so as to enable simulations of large porous domains. Pore scale models that preserve the fine scale resolution include lattice Boltzmann methods, particle methods or grid-based direct numerical simulation methods. This group of approaches has faced a computational limitation in terms of the size of domains that can be simulated.

An approach that does not fall in these two broad categories, but has also been successfully applied in some pore scale studies is the so-called micro-continuum approach. In this approach, continuum model concepts are applied to very small volumes of porous medium (micron scale), often at the scale where pore scale processes take place (e.g., Noiriel et al. 2012; Carroll et al. 2013).

Models that combined different approaches for various components of the model have also been employed. Mixed approach models are usually developed for practical reasons: to take advantage of existing, time-tested methods or software packages, or because specific approaches are computationally advantageous. For example, conventional discretization methods have been used to simulate pore scale processes when a solution of the flow field was obtained with a lattice Boltzmann method (Yoon et al. 2012), or a random walk method has been used for reactive transport while a direct finite difference solver was used for Navier Stokes flow (Sadhukhan et al. 2012).

The dynamics of physical and chemical processes at the continuum scale are controlled by phenomena that take place in a localized region of the domain where the continuum scale models break down and resolving the pore scale is necessary. However, in most of the domain, the computationally demanding pore scale resolution is not necessary. Hybrid multiscale models (Scheibe et al. 2007), where the different spatial scales are resolved in different parts of the domain, can be used to overcome the limitations regarding the size that “brute force” pore scale models would require. Pore scale and continuum scales are coupled by enforcing the continuity of pressures and mass fluxes at the pore/continuum interfaces (Battiato et al. 2011). Coupling between subdomains can be done using finite-element spaces to determine interface conditions, such as in the mortar method (Balhoff et al. 2008). Mortar coupling is a domain decomposition approach in which subdomain are coupled together using a low-degree of freedom mortar space defined on a coarse grid in such a way that fluxes match weakly. Mortars have been used primarily for coupling continuum-scale models, but were recently extended to model flow at multiple spatial scales (Balhoff et al. 2008) and applied to upscale reactive transport processes associated with CO₂ sequestration using a pore network model as the underlying pore scale model (Mehmani et al. 2012). Another approach to multiscale CO₂ modeling is that of (Varloteaux et al. 2013), where pore network model simulations are used to evaluate continuum scale parameters as the pore space evolves due to geochemical processes. We are not aware of the existence of any adaptive hybrid multiscale model, an approach in which the pore scale description would be adaptively applied where needed depending on the physical or chemical evolution of the system (e.g., where sharp geochemical gradients exist).

Pore network models

In pore network models, the pore space geometry is conceptualized as a network of pore volumes connected by channels or pore throats (Fatt 1956; Payatakes et al. 1973) (e.g., Fig. 16). Mass fluxes are calculated for each channel or pore throat and a mass balance equation is solved at each pore volume. For flow of a single phase fluid, the mass balance in the i^{th} pore volume can be written as a sum of fluxes from all pore volumes j connected to i , q_{ij} (e.g., Mehmani et al. 2012):

$$\sum_j q_{ij} = \sum_j G_{ij} (P_i - P_j) = 0 \quad (37)$$

where P_i and P_j are the fluid pressures, and G_{ij} is a coefficient that is a function of the properties of the connection. Often specific geometrical shapes are used for the connection and G_{ij} has a definite form e.g., $G_{ij} = (\pi r_{ij}^4 / 8\mu L_{ij})$ for a cylinder of radius r_{ij} and length L_{ij} as in Mehmani et al. (2012). In general, the major practical challenge of single phase pore network models is to find accurate way of representing real porous media. For that, the structure of the pore network can be extracted from 3D images such as those obtained from XMCT (e.g., Bauer et al. 2012; Varloteaux et al. 2013). Pore network extraction based on skeletonization using a medial axis analysis is a common approach in the work of Lindquist and co-workers (Lindquist and Venkatarangan 1999; Lindquist et al. 2000; Kim et al. 2011). Other techniques, such as the distance ordered homotopic thinning technique (Pudney 1998; Bauer et al. 2012), have also been used for pore network extraction.

The mass balance of each species subject to reactive transport can be written for each pore of volume V_i (e.g., Kim et al. 2011)

$$V_i \frac{\partial C_k}{\partial t} = \sum_{q_{ij}>0} q_{ij} C_{k,j} + \sum_{q_{ij}<0} q_{ij} C_{k,i} + \sum_j DA_{ij} \frac{C_{k,j} - C_{k,i}}{L_{ij}} + V_i R_{k,i} \quad (38)$$

where $R_{k,i}$ is the reaction rate contribution to component k in the i^{th} pore volume, and A_{ij} is the cross-sectional area of the throat.

If mineral precipitation-dissolution is considered, the volume change of the pores can be calculated and translated into a change in the conductance G_{ij} of the connection. Different assumptions are made in translating this volume change and conductance change (see for example Mehmani et al. 2012; Varloteaux et al. 2013), but the resulting simulations make it possible to

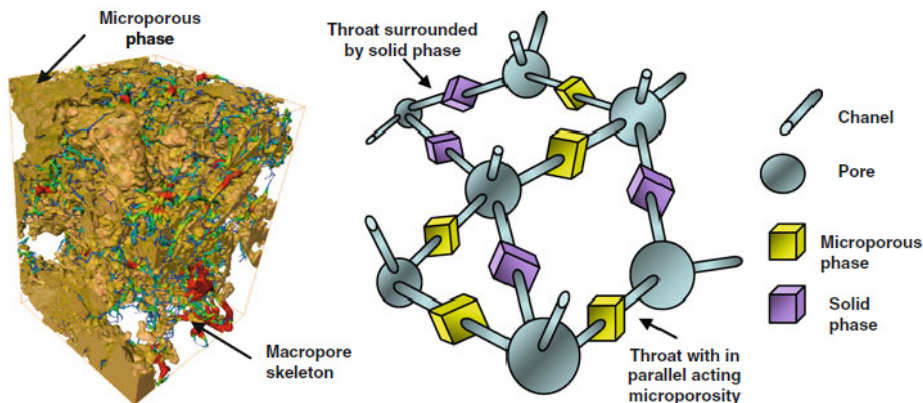


Figure 16. Dual pore network conceptualization (right) for a carbonate rock sample (left) with micro and macroporosity domain (Bauer et al. 2012).

evaluate feedback processes between reactions and flow at larger scales under different reactive transport regimes. Heterogeneous mineral distributions can also be incorporated in pore networks based on XCMT image analysis (Kim et al. 2011).

Due to the computational challenges associated with pore scale models based on a direct representation of the pore space and the fluid-fluid interfaces, pore network models are by far the most common approach for simulating multiphase flow in the literature. However, applications to CO₂ injection and sequestration are lagging behind other applications such as oil reservoirs and other environmental applications. Comprehensive reviews of quasi-static and dynamic multiphase pore network models are provided in Blunt (2001), Blunt et al. (2002, 2013), and Joekar-Niasar and Hassanizadeh (2012). Blunt et al. (2013) recognized that for multiphase flow, network modeling offers the most proven approach for predicting relative permeability and capillary pressure. In Blunt et al. (2013), imaging, network extraction, assignment of contact angle and pore network simulation of displacement of water by a non-wetting phase (oil) on three carbonates samples are presented.

Kang et al. (2005) applied the invasion percolation theory in a pore network to two-phase immiscible displacement of seawater by liquid CO₂ in deep oceanic sediments. The invasion percolation theory was used to model the slow immiscible displacement controlled by capillary forces of two phases within a porous medium where a non-wetting phase such as CO₂ displaces a wetting phase. In the system considered by Kang et al. (2005), CO₂ and seawater are assumed to react to form hydrate and the depth of CO₂ invasion in the sediments is controlled by changes in the pore-scale porosity close to the hydrate formation front. The effects of contact angle heterogeneity on CO₂ saturation involving quartz and mica were modeled in 2D and 3D pore networks over a range of viscosity ratios (M) and capillary numbers (Ca) relevant to carbon sequestration (Ellis and Bazylak 2012, 2013).

Lattice Boltzmann method

Rather than solving the conservation equations for the concentrations or momentum directly, the lattice Boltzmann (LB) method simulates the fluid/s as consisting of particles on a discrete lattice that perform consecutive propagation and collision steps. The LB method recovers the macroscopic pore-scale equations (e.g., Navier-Stokes) and is easily parallelizable.

The Bhatnagar-Gross-Krook (BGK) collision operator (Bhatnagar et al. 1954) is commonly used in the discrete Boltzmann equation:

$$f_i(\mathbf{x} + \mathbf{e}_i \Delta t, t + \Delta t) - f_i(\mathbf{x}, t) = -\omega (f_i(\mathbf{x}, t) - f_i^{eq}(\mathbf{x}, t)) \quad (39)$$

where f_i is the discrete particle distribution function and Δt is the time step size. The term on the left hand side expresses the propagation of particles according to the lattice velocity \mathbf{e}_i , a set of vectors which depend on the choice of lattice. The term on the right-hand side represents the BGK rule for collision. The BGK collision expresses how the particle distribution f_i relaxes to the local equilibrium distribution function f_i^{eq} with a single relaxation frequency ω . The relaxation frequency determines the kinematic viscosity of the fluid, e.g., $\nu = c_s^2(1/\omega - 1/2)$ in Kang et al. (2005). The form of the local equilibrium distribution function f_i^{eq} depends on the macroscopic equations that one wants to recover and the order of accuracy desired.

The LB method has the advantage of describing non-equilibrium dynamics, especially in fluid flow applications involving interfacial dynamics and complex boundaries (Chen and Doolen 1998). For multiphase flow, most lattice Boltzmann models (e.g., Shan and Doolen 1995) treat the interface as a diffuse one, where for the case of an immiscible binary mixture at equilibrium the two fluids are separated by an interface of finite thickness.

Complex fluid-solid interfaces are usually treated with a bounce back boundary condition. Kang and co-workers have applied the LB method to reactive transport problems (e.g., Kang

et al. 2007), with consideration of aqueous speciation reactions and the evolution of the pore space geometry as a result of precipitation-dissolution. Hiorth et al. (2013) constructed a LB model that includes non-linear dissolution-precipitation kinetics, surface complexation, and ion exchange and applied to the injection of seawater into a chalk core. Chen and Zhang (2010) simulate density driven convection driven by the dissolution of scCO_2 in the brine occupying the pore space of a single fracture. Model results show that after the onset of convective instability, the increase in the interfacial area between CO_2 -rich brine and unaffected brine may favor the migration of CO_2 into the fracture and adjacent porous medium.

Although the works mentioned above have been limited to rather simple geometries and 2D problems (Kang et al. 2007; Chen and Zhang 2010), recent lattice Boltzmann studies dealing with immiscible multiphase reactive systems in complex 3D porous geometries (Parmigiani et al. 2011) show that the LB method is capable of addressing the requirements of computational pore scale simulations of CO_2 injection and sequestration (Fig. 5a).

Particle methods: Smooth particle hydrodynamics and moving particle

In particle methods such as the smooth particle hydrodynamics method (SPH) and moving particle method (MPS), fluids are represented by N_p particles with intensive properties (e.g., mass m_i) that are tracked in time as they move in the pore space. Continuous variables (e.g., density) are represented as the superposition of kernel functions centered on a set of discrete particle points \mathbf{r}_i . In continuous form, this superposition for variable $A(\mathbf{r})$ at point \mathbf{r} can be expressed in integral form as

$$A(\mathbf{r}) = \int A(\mathbf{r}')W(\mathbf{r} - \mathbf{r}', h)d\mathbf{r}' \quad (40)$$

where W is the kernel and the parameter h is the kernel size that defines the domain of influence of the kernel for each particle. To reduce the computational costs in numerical calculations, the domain of influence is chosen to be finite such that $W(\mathbf{r} - \mathbf{r}', h) = 0$ when $|\mathbf{r} - \mathbf{r}'| > h$. In SPH, the kernel function satisfies $\int W(\mathbf{r} - \mathbf{r}', h)d\mathbf{r}' = 1$ and the discrete approximation to $A(r)$ at particle point r_i is

$$A(\mathbf{r}_i) \approx A^*(\mathbf{r}_i) = \sum_i^{N_h} A^*(\mathbf{r}_j)W(|\mathbf{r}_i - \mathbf{r}_j|) \quad (41)$$

where N_h is the number of particles within the region defined by h . In the moving particle method, the kernel function does not necessarily need to satisfy the normalization conditions, however, for convenience we will not present these expressions here. The gradient of the continuous field $A(r)$ can also be written as a function of the kernel functions

$$\nabla A(\mathbf{r}_i) \approx A^*(\mathbf{r}_i) = \sum_i^{N_h} A^*(\mathbf{r}_j)\nabla W(|\mathbf{r}_i - \mathbf{r}_j|) \quad (42)$$

Variables in the equations describing fluid flow, transport and reactions and their gradients are discretized as particle equations using Equations (41) and (42). As a result, the discretized forms of the differential equations are a function of the relative position of the particles $W(\mathbf{r}_i - \mathbf{r}_j, h)$, and the kernel function W . The kernel function is in practice defined as a spline or polynomial function defined piece-wise between $0 < |\mathbf{r}_i - \mathbf{r}_j| < h$.

Particle methods have recently been applied to the simulation of multiphase flow involving CO_2 and brine (Bandara et al. 2011) and multicomponent transport associated with elevated CO_2 and SO_2 concentrations (Ovaysi and Piri 2013). Bandara et al. (2011) developed an SPH model for multiphase CO_2 -brine flow. Rather than prescribing an interface between fluids, fluid-fluid and fluid-fluid-solid interfaces are simulated via an approach similar to molecular dynamics in which a combination of short repulsive and medium range attractive forces are included, leading to a diffuse interface. These forces are added in the momentum balance equation according to

$$\frac{\partial(m_i \mathbf{u}_i)}{\partial t} = \mathbf{F}_i + \mathbf{F}_i^{\text{interaction}} \quad (43)$$

$$\mathbf{F}_i^{\text{interaction}} = \sum_j \mathbf{F}_{i,j}^{\text{interaction}} \quad (44)$$

The form of $\mathbf{F}_{i,j}^{\text{interaction}}$ ensures that it is repulsive in the short range, attractive in the medium range and zero when particles i and j are separated by a distance greater than h :

$$\mathbf{F}_{i,j}^{\text{interaction}} = \begin{cases} s_{ij} \cos\left(\frac{3\pi}{2h}|\mathbf{r}_i - \mathbf{r}_j|\right) \frac{\mathbf{r}_i - \mathbf{r}_j}{|\mathbf{r}_i - \mathbf{r}_j|} & |\mathbf{r}_i - \mathbf{r}_j| \leq h \quad |\mathbf{r}_i - \mathbf{r}_j| \leq h \\ 0 & |\mathbf{r}_i - \mathbf{r}_j| > h \end{cases} \quad (45)$$

where s_{ij} is the strength of the particle-particle interaction. In this model, the immiscible behavior of the CO₂ and brine phases is simulated with the interaction strengths between particles of same type (s_{ij}) larger than that of different fluids (brine and CO₂). Wetting and non-wetting are represented by a set of stationary particles that have different strengths s_{solids} with respect to brine or CO₂. With this method, Bandara et al. (2011) were able to reproduce the processes by which isolated CO₂ bubbles are left trapped in the pore space: division, leave behind, snap-off (Fig. 5b), and coalescence.

Ovaysi and Piri (2013) used a modified moving particle method to simulate multicomponent advection, diffusion, and electrochemical migration of CO₂ and SO₂, while also considering aqueous equilibrium complexation reactions associated with these species. The simulation was performed on a domain generated from microtomographic images of Berea and Bentheimer sandstones.

Although a significant body work exists in the application of SPH in reactive systems with mineral-precipitation processes that result in evolving pore geometry, in particular by A. Tartakovsky and co-workers (Tartakovsky et al. 2007a,b), widespread application of this method to CO₂ problems is still not available in the literature. The ability of particle methods to simulate processes with dynamically evolving interfaces, e.g., fluid-solid (Tartakovsky et al. 2007a,b), fluid-fluid-solid employing methods akin to molecular dynamics (Bandara et al. 2011), or fluid-fluid with the Cahn-Hilliard diffuse interface theory (Xu et al. 2009) suggest they are a useful tool to address coupled simulation of the physical and chemical processes associated with CO₂ injection and sequestration. However, one of the main challenges faced by particle methods is the size of problems that can be addressed. The simulations by Bandara et al. (2011) and Tartakovsky et al. (2007a,b) were performed on 2D domains with mineral grains represented as circular shapes, while the work of Ovaysi and Piri (2013) simulates a relatively small domain (0.51×0.51×1.09 mm). This challenge can be overcome with the use of massively parallel implementations such as in the recent application for single-component conservative transport in a 3D sphere pack of dimensions 2×2×4 mm (Scheibe et al. 2013).

Direct numerical simulation

Direct numerical simulation involves the use of conventional discretization methods to solve the flow, transport and geochemical equations introduced in earlier sections. These Eulerian, mesh-based methods include finite volume, finite differences and finite element methods (Patankar 1980; de Marsily 1986; Zienkiewicz et al. 2005). Complex geometries of the pore space that do not evolve with time can be captured well and simulated efficiently with the mesh-based methods. However, pore scale processes associated with CO₂ sequestration involve multiple evolving interfaces. Specific methods must be employed to capture within the resolution of the discretization the moving interfaces. These methods can be broadly classified between those that track the interface, such the volume-of-fluid method for multiphase processes (Huang et al. 2005; Huang and Meakin 2008; Raeini et al. 2012), or the embedded

boundary methods for mineral-fluid interfaces (Miller and Trebotich 2012; Molins et al. (2012) (see Fig. 17), and those that mark both sides of the interface by means of a level set function e.g., for geometry update (Li et al. 2008, 2010) or a phase-field variable, e.g., for geometry evolution (Xu and Meakin 2008, 2011) or for multiphase flow according to the Cahn Hilliard model (Bogdanov et al. 2011).

While multiphase application of direct numerical simulation methods to the processes that take place in petroleum reservoirs are more common (e.g., Raeini et al. 2012), applications to the CO₂ problem are mostly work in progress. The effect of a single phase flow of a solution rich in CO₂ on the dissolution of calcite in a 0.5×0.5×1.5 mm 3D geometry of packed spheres has been studied by Flukiger and Bernard 2009) using a finite volume method.

EMERGENT PROCESSES

Physical evolution of the pore space

As a result of dissolution or precipitation associated with CO₂ injection and sequestration, the mineral surface evolves with time, thus modifying the pore space. Assuming uniform dissolution-precipitation of a single mineral phase the velocity of the moving interface \mathbf{u}^Γ can be described by (e.g., Li et al. 2010)

$$\mathbf{u}^\Gamma \cdot \mathbf{n} = \frac{\bar{r}}{\rho_m} \quad (46)$$

where ρ_m is the molar density of the mineral phase and \bar{r} is the reaction rate.

As a result of these changes in the pore space, the flow paths available for the transport of reactants evolve with time. Evolution of the flow paths in turn may hinder further reaction progress in the case of clogging or enhance it by opening new flow channels. This pore space evolution depends on the relative importance of reactive and transport processes. The Damköhler numbers are usually employed to evaluate the relative importance of transport and reactions (see Eqns. 16 and 17). The length scale for pore scale studies is typically given by the grain or pore size, which suggests that kinetics and diffusion become increasingly important at these and smaller scales—the local equilibrium assumption, for example, is much harder to justify as a general approach at the pore scale.

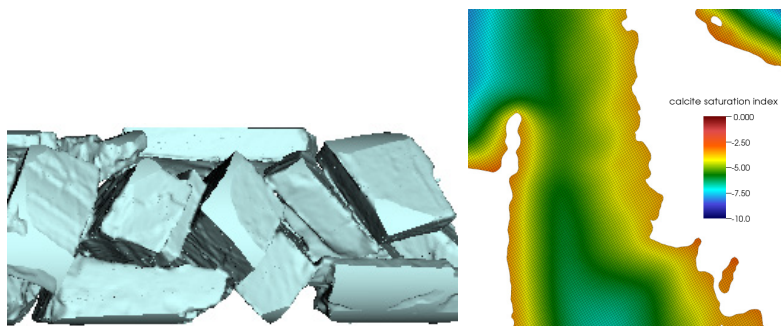


Figure 17. (a) Portion of the computational domain constructed from XCOM data showing mineral grains (~200 μm in size) represented as embedded boundaries on a Cartesian grid using the methods in Trebotich et al. (2008) and Molins et al. (2012). The capillary tube was 0.7 cm in length and 0.5 mm in diameter, with approximately 1.3 billion grid points used to provide a spatial resolution of 1.12 μm . (b) Diffusion boundary layer around dissolving calcite grain as shown by the calcite saturation index ($\log Q/K_{\text{eq}}$) in the solution in the pore space (Molins et al. 2012).

A well-known phenomenon is that of formation of wormholes as a result of the reactive infiltration instability (Ortoleva et al. 1987; Hoefner and Fogler 1988; Steefel and Lasaga 1990; Daccord et al. 1993; Fredd and Fogler 1998; Steefel and Maher 2009; Smith et al. 2013a). In this emergent process, mineral dissolution under transport-controlled conditions leads to the more rapid growth of high flow velocity pathways over slower pathways. This is a form of geochemical self-organization or pattern formation that is characteristic of advection-dominant (high Péclet number) reactive flow systems. As shown experimentally by Hoefner and Fogler (1988) and computationally by Steefel and Lasaga (1990) and Steefel and Maher (2009), the wormholes become more highly ramified and ultimately diffuse when the Damköhler number is small (surface reaction-controlled) for a given system.

The injection of CO₂ at depth drives the subsurface environment into far from equilibrium, undersaturated conditions, similar to the environment in the near-well bore region when matrix acidization is used for the purposes of permeability enhancement (Cohen et al. 2008). Smith et al. 2013a) demonstrated that wormholing of a caprock sample consisting of dolomite and anhydrite occurred when CO₂-acidified solution was injected. Heterogeneous dissolution at the pore scale has been observed in experiments performed under conditions relevant for CO₂ sequestration: at pCO₂ = 10 MPa and 100 °C for an oolitic limestone from the Mondeville formation (Paris basin, France) (Luquot and Gouze 2009) and at pCO₂ = 3 MPa and 60 °C for a Vuggy limestone from the Weyburn-Midale field, Saskatchewan, Canada (Carroll et al. 2013). At lower pCO₂ values (0.7 MPa), such features are not observed for the same oolitic limestone from the Mondeville formation (Luquot and Gouze 2009). Heterogeneous dissolution was not observed at pCO₂ = 3 MPa and 60 °C for a Midale Marly dolostone from the Weyburn-Midale field that contained a much higher abundance of dolomite relative to calcite and higher initial porosity and permeability compared to the Vuggy limestone (Carroll et al. 2013), although this is likely due to the combination of slower reaction kinetics and smaller experimental length scales such that the effective Damköhler number remains small (Fig. 11). Carroll et al. (2013) proposed that their data could be described by a porosity-permeability relationship of the form

$$k = k_o \left(\frac{\phi}{\phi_o} \right)^3 \quad (47)$$

that captures the evolution of permeability associated with reaction-induced porosity (ϕ) change.

A number of different formulations have been used for a porosity-permeability relationship in reactive rocks, although it should be pointed out that few have been tested carefully against reaction-induced (either dissolution or precipitation) permeability change. Exceptions are the experimental study of Armstrong et al. (2012) and the computational study of Molins et al. (2011). In modeling studies of reaction-induced porosity and permeability change (note that we do not specifically focus on CO₂ here, since the behavior should be fairly general for acidified brines when the dissolution of carbonate is involved), the Kozeny-Carman equation was used by Steefel and Lasaga (1990) to simulate wormholing

$$k = C_k \frac{\phi^3}{(1-\phi)^2 S^2} \quad (48)$$

where S is the surface area of the solids per unit volume solids, and thus proportional to the inverse of the average grain diameter (Bear 1988). An equivalent formulation is based on a specification of the initial porosity and permeability

$$k_t = k_o \frac{(\phi_t)^3}{(1-\phi_t)^2} \frac{(1-\phi_o)^2}{(\phi_o)^3} \quad (49)$$

where the subscript t refers to the permeability or porosity over time and the subscript 0 refers to the initial permeability or porosity. For rocks in which the porosity and permeability is dominated by approximately planar fractures, a cubic law relationship has been proposed and used (Phillips 1991; Steefel and Lasaga 1994; Steefel and Lichtner 1998)

$$k = \frac{\phi_f \delta^3}{12} \quad (50)$$

where ϕ_f is the fracture porosity and δ is the average fracture aperture. Other formulations have been proposed, included a simple power law relationship (Noiriel et al. 2004)

$$k \propto \phi^n \quad (51)$$

with the exponent n decreasing continuously with time as dissolution of the microcrystalline phase progressed as a result of injection of CO_2 -rich, acidic solution. The same concepts can be used to model the permeability of caprock fractures (Ellis et al. 2011; Deng et al. 2013; Elkhoury et al. 2013) as discussed by Fitts and Peters (2013, this volume).

In the Noiriel et al. (2004) study, once the microcrystalline phase in the limestone was locally depleted, dissolution shifted to the sparitic phase, resulting in a constant value of the constant n and a decrease in the roughness of the pore walls as recorded by XCMT analysis (Fig. 18).

Another set of limestone dissolution experiments that coupled XCMT to quantify pore structure changes with solution effluent analysis were undertaken by Luquot and Gouze (2009). They carried out experiments at three different flow rates, resulting in three different Damköhler numbers as evaluated across the length of the core sample. At the highest flow rate (and thus lowest Damköhler number designated as D3), no gradients in porosity developed—dissolution was effectively homogeneous over the length of the core (Fig. 19).

As discussed initially by Hoefner and Fogler (1988) and Steefel and Lasaga (1990), the case of low Damköhler number flow and reaction results in diffuse reaction with little tendency to “wormhole”. At lower flow rates and higher Damköhler number, Luquot and Gouze (2009)

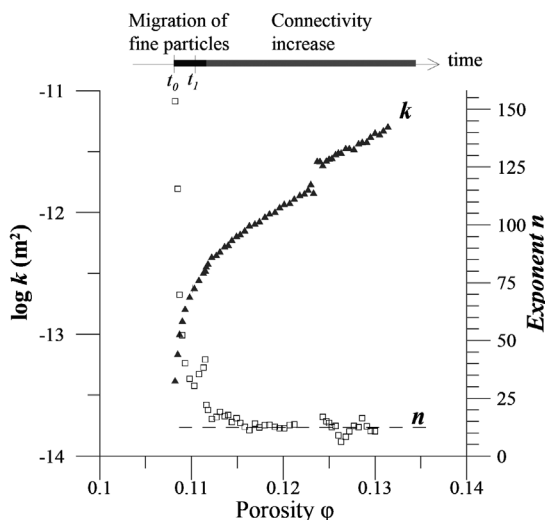


Figure 18. Permeability (log axis) and power law exponent n versus porosity for CO_2 -induced dissolution of a limestone (Noiriel et al. 2004).

demonstrated that gradients in reaction developed and the dominant dissolution feature were fingers or wormholes that resulted in highly heterogeneous porosity development. XCOMT images of the three Damköhler regimes ($D1 > D2 > D3$) investigated in the study are shown in Figure 20, in this case with the range in the Damköhler number resulting from the use of different flow velocities (in contrast to the study by Carroll et al. (2013), where reactivity was the adjustable parameter).

Analyzing these experimental results, Guze and Luquot (2011) concluded that the low Damköhler experiment in which the dissolution was homogeneous resulted in a decrease in tortuosity, while the higher Damköhler number experiment (heterogeneous porosity develop-

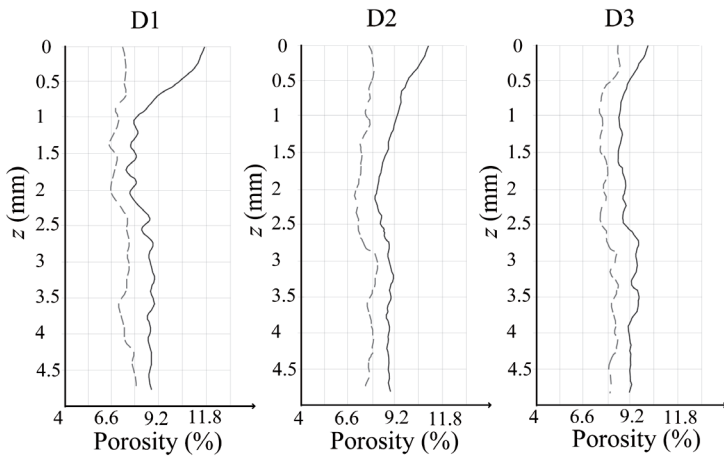


Figure 19. X-Y averaged porosity profiles for three different Damköhler numbers ($D1 > D2 > D3$), with pre-experiment results shown with a dotted line, post-experiment results shown with a solid line (Luquot and Guze 2009).

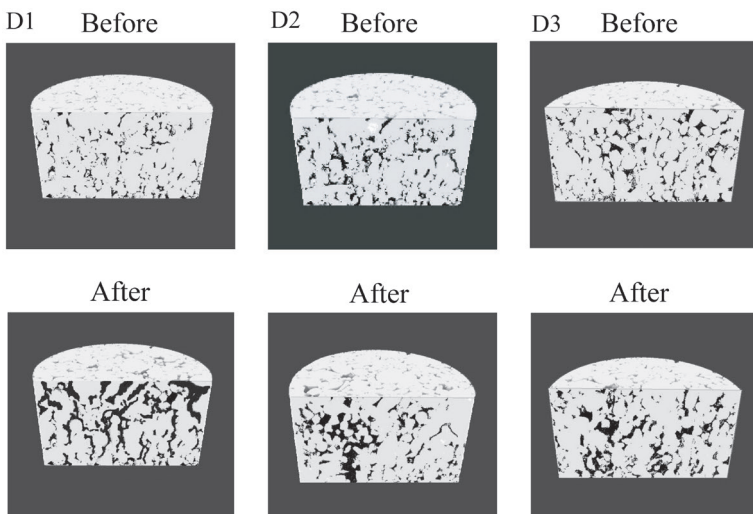


Figure 20. XCOMT before and after injection of a CO_2 -acidified solution for the 3 Da numbers (Luquot and Guze 2009).

ment) also resulted in a tortuosity decrease, but accompanied by an increase in hydraulic radius. They proposed a porosity-permeability relationship based on a percolation threshold in which a critical porosity, ϕ_c , is defined

$$k(t) = k_o [\phi(t) - \phi_c]^\alpha \left(\frac{B_\tau}{\tau} \right) \quad (52)$$

where α is the power dependence of the relationship that typically varies over time, τ is the tortuosity and B_τ is an experimentally determined coefficient. Based on their experimental data, they estimated a critical porosity corresponding to the percolation threshold of 5.9%. Carroll et al. (2013) pursued this general approach of combining XCMT to quantify pore structure changes with effluent chemistry to determine bulk reaction rates.

Chemical evolution of the pore space: reactive surface area

The reaction rate in Equation (36) and (46) is expressed per units of physical interfacial area between the mineral and the fluid phase. It can be related to the actual rate r in Equation (33) (per units of reactive surface area) via a parameter ψ (m^2 physical surface m^{-2} reactive surface). For a surface with a heterogeneous mineralogy, ψ represents the portion of surface with mineral reactions, but ψ can also be used to represent enhanced reactivity due to surface roughness not resolved at the pore scale, i.e., nanometer scale roughness, or atomic scale density of reactive sites (Bracco et al. 2013). The reactive surface area has traditionally been estimated from adsorption isotherms (Brunauer-Emmett-Teller, or BET) (Brunauer et al. 1938) or geometrically based on the average physical grain size. However, these approaches do not account for the hydrologic accessibility of the reactive phases within the pore structure (Peters 2009; Landrot et al. 2012).

In a study by Noiriél et al. (2009) of limestone infiltrated by CO_2 -rich solution, Sr and Ca release rates were used to assess the relative dissolution rates of the sparitic and microcrystalline phases in the limestone subjected to infiltration of CO_2 -rich solution. The results demonstrate that the RSA of the sparite in this case increased greatly, as recorded by the rate of dissolution of that phase over time. In contrast, its geometric surface area, as recorded by XCMT, decreased slightly. To describe the time dependent behavior, Noiriél et al. (2009) proposed a “sugar cube” model in which disaggregation of the granular network (presumably resulting in the large increase in RSA of the sparitic phase, which is now exposed to more of the reactive infiltrating solution) precedes dissolution of the individual grains of sparite. Noiriél et al. (2009) described the time-dependent RSA, Sr, mathematically with the expression

$$S_r = \left(S_{r0} + S_{rm} \left[1 - \left(\frac{C}{C_0} \right)^{n_1} \right]^{n_2} \right) \left(\frac{C}{C_0} \right)^{n_3} \quad (53)$$

where S_{r0} is the initial surface area, S_{rm} is the maximum surface area given by the sum of all of the surface areas of the individual particles, C is the concentration of the mineral calcite over time, C_0 is its initial concentration, and n_1 , n_2 , and n_3 are empirical coefficients that depend on the geometry of the aggregate.

Focusing on the low Damköhler case (D3) in which reaction rates over the length of the core are largely homogeneous, Luquot and Gouze (2009) proposed an expression for the average effective reactive surface area (m^2 mineral m^{-3} porous medium) over time, $\bar{\sigma}(t)$

$$\bar{\sigma}(t) = \bar{\sigma}^* \left(\frac{\bar{\phi}(t)}{\bar{\phi}^*} \right)^{-w} \quad (54)$$

where $\bar{\sigma}^*$ and $\bar{\phi}^*$ are the initial reactive surface area and the porosity, respectively, and w is an

experimentally-determined positive coefficient. This leads to an expression for the porosity change with time Luquot and Gouze (2009) of the form

$$\bar{\phi}(t) = \bar{\phi}^* (1 + A(w)t)^{1/w} \tag{55}$$

with the coefficient $A(w)$ is given by

$$A(w) = \bar{r}' \bar{\sigma}^* v w \tag{56}$$

where w and \bar{r}' (the average reaction rate) characterize the reaction regime and v is the molar volume of calcite. According to these expressions, this leads to an evolution of the reactive surface area in the limestone for the three Damköhler cases shown in Figure 21.

For the case of carbonate precipitation that occurs when carbonate-forming metal cations and alkalinity are available from either mineral dissolution or the local brine, Noiriél et al (2012) investigated the change in reactive surface area using two approaches: 1) based on XCMT mapping of mineral-fluid interfaces, and 2) based on the ability to capture time-dependent reactivity with a micro-continuum model. Based on an XCMT analysis using a voxel size of 4.4 microns at the Advanced Light Source (Lawrence Berkeley National Laboratory), surface area was determined geometrically by counting the interfaces between solid (either glass spheres or calcite spar) and fluid (porosity). The data show a distinct nucleation or surface roughening event between the column inlet and a distance of about 2 mm downstream in the core (Fig. 22), a result consistent with the fact that the supersaturation was highest in this portion of the column (which gradually decreases downstream as a result of reaction).

The conclusion that reactive surface area increased locally in the column due to nucleation and/or crystal growth was reinforced by micro-continuum modeling results using the code CrunchFlow (Noiriél et al. 2012). Figure 23 contrasts the ability of the micro-continuum model to capture the increase in calcite volume fraction based on the XCMT. The panel on the left uses only the initial BET-determined specific surface area value of 0.012 m²/g for the calcite and thus underpredicts significantly the amount of carbonate accumulated in the first 2 mm of the column (supersaturated solution is injected from the left). In contrast, the panel on the right uses a specific surface area value of 0.21 m²/g for newly formed calcite based on a post-experiment five point krypton BET analysis. Note that the modeling here is based entirely

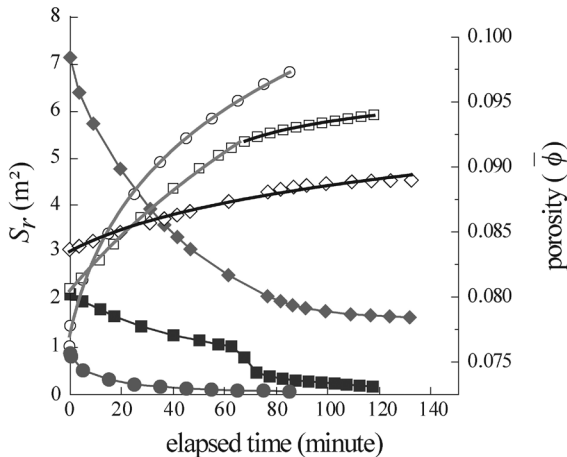


Figure 21. Reactive surface area (S_r , filled symbols) and porosity (ϕ , empty symbols) versus elapsed time for experiments D1 (circles), D2 (squares), and D3 (diamonds) investigated by Gouze and Luquot (2011).

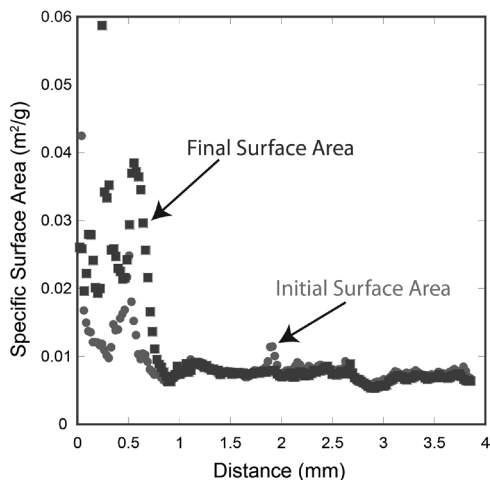


Figure 22. Nucleation or surface roughening event with 2 mm of the column inlet, which was injected with a supersaturated solution of sodium bicarbonate and calcium chloride (Noiriel et al. 2012). The initial specific surface area based on the XCMT mapping is shown as solid circles, while the final specific surface area is represented by solid squares.

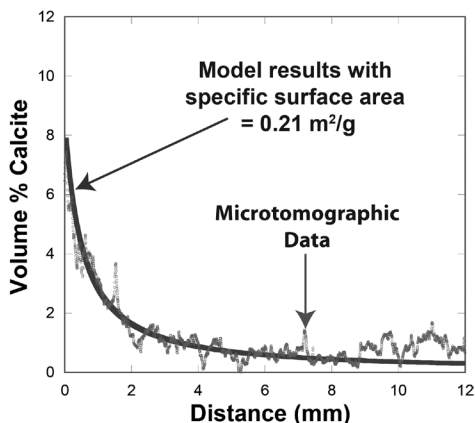
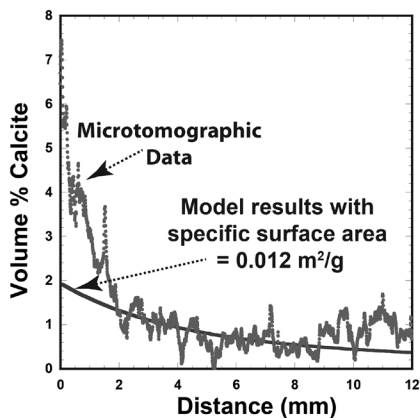


Figure 23. Comparison of micro-continuum modeling of the accumulation of calcite (volume %) using the code CrunchFlow for the case in which a specific surface based on the initial BET determination on unreacted calcite spar (Left Panel) and for the case in which a higher specific surface area based on post-experiment BET determination is used. The results do not involve any fitting of the microtomographic data, as they make use of independently determined parameters (rate constants, BET surface area, porosity). The results demonstrate the importance of the spatial and temporal evolution of reactive surface area (Noiriel et al. 2012).

on independently determined parameters and makes no attempt to calibrate these parameters based on the XCMT data.

CO₂ invasion

The invasion of CO₂ in the brine-saturated porous medium is an energetically unfavorable process due to the low viscosity ratio (M) between CO₂ and brine. Under these conditions, the front propagation during the immiscible displacement is unstable, and fingering, an emergent process, is observed. Depending on the dimensionless capillary number (Ca), capillary fingering or viscous fingering may develop. Capillary fingering takes place when the capillary force of the wetting fluid is the dominant force and is characterized by fluid phase geometries characterized by wider lateral nonwetting (CO₂) phase flowpaths. Viscous fingering takes place

when the viscous driving force of the nonwetting fluid is lower and is characterized by narrow flowpaths that propagate forward rather than laterally. Figure 24 illustrates viscous fingering (top left) and capillary fingering (bottom left) compared to stable displacement (top right) in the Pore Network simulations of Ellis and Bazylak (2013).

Micromodel experiments by Wang et al. (2013) showed that capillary fingering was the dominant mechanism for all scCO₂ injection rates in a continuous-rate experiment, where the rate was increased after quasi-steady conditions were reached for a given injection rate. However, in a discontinuous-rate injection, where the micromodel was saturated with brine before each scCO₂ injection rate was imposed, crossover from capillary to viscous fingering was observed for logCa = -5.91 to -5.21. This resulted in a large decrease in scCO₂ saturation. The discontinuous-rate experimental results confirmed the decrease in nonwetting fluid saturation during crossover from capillary to viscous fingering predicted by numerical simulations carried out by Lenormand et al. (1988).

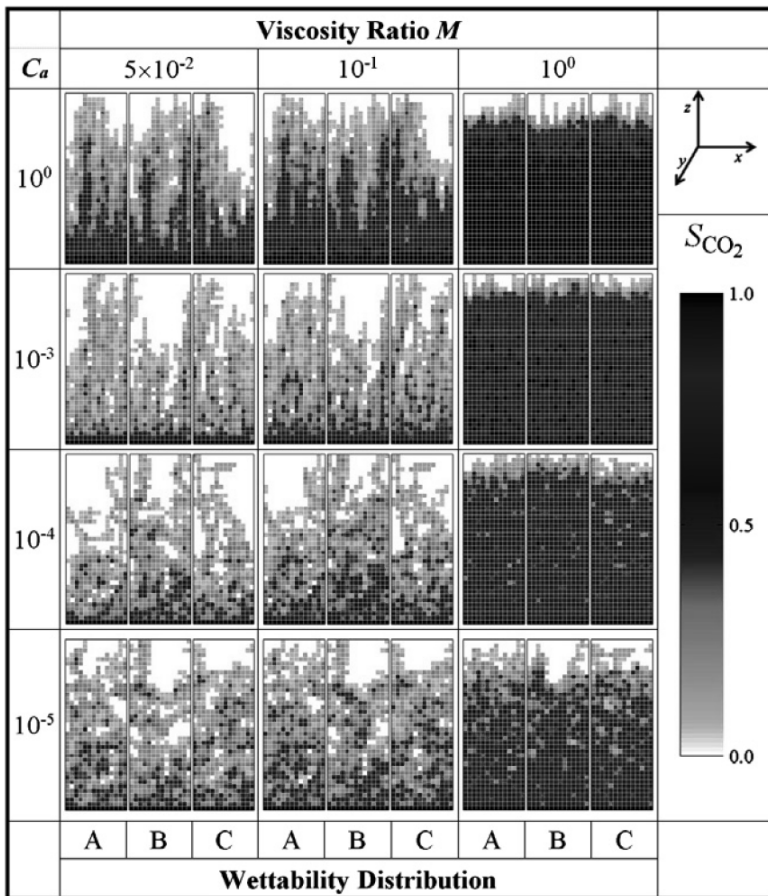


Figure 24. Pore network simulation results from Ellis and Bazylak (2013) showing the saturation patterns for various Ca , M , and wettability conditions A (homogeneous), B (heterogeneous), and C (homogeneous). The grey scale values indicate the averaged relative CO₂ saturation in the direction normal to the page. The bottom face is the inlet in each case, and the mean pore diameter is 5 μm . (The reader is referred to the web version of this article for a color version.)

While the experiments by Wang et al. (2013) were for a homogeneous medium, heterogeneity can have a significant effect on CO₂ invasion. Zhang et al. (2011) investigated liquid CO₂ (LCO₂) water displacement in a pore network micromodel with two distinct permeability zones. LCO₂ displaced water only in the high permeability zone at low injection rates, while at high injection rates, LCO₂ displaced water in the low permeability zone with capillary fingering as the dominant mechanism. Microtomographic images of the distribution of CO₂ in a flooding experiment by Blunt et al. (2013) suggests that CO₂ is trapped in the pore space surrounded by brine as clusters of all sizes, from small blobs in the center of a single pore to ramified, extensive ganglia spanning several pores.

Using pore network modeling of multiphase flow, Ellis and Bazylak (2013) investigated the effects of contact angle heterogeneity on CO₂ saturation (S_{CO_2}) in a system containing quartz and mica over a range of viscosity ratios (M) and capillary numbers (Ca) relevant to carbon sequestration (Fig. 24). Simulations showed that at $Ca = 10^{-4}$, CO₂ saturations were 20% higher for heterogeneous contact angle distributions compared to similar networks with homogeneous distributions. The results were quantified based on a power law correlation similar to that proposed by Al-Fossail and Handy (1990) relating the dimensionless M to the brine saturation. The power-law expression has the form

$$S_{\text{CO}_2} = AM^n \quad (57)$$

where A and n are fitting parameters. Good qualitative agreement was found between fitted curves and simulated results, with fitting parameters differing between homogeneous and heterogeneous cases only at low capillary numbers.

NEW DIRECTIONS

Despite the length of this chapter, in fact the research into pore scale processes associated with CO₂ injection and sequestration has only just scratched the surface of the topic. Much remains to be done to achieve a mechanistic understanding of the pore scale processes that could be captured in a defensible predictive model. The field is clearly far from mature. For example, the characterization of pore scale physical and chemical properties at sufficiently high resolution that the data can be incorporated into true pore scale models is only just beginning—collecting 3D geochemical data at high spatial resolution is arguably the biggest challenge here. While the resolution available for mapping of the physical structure of porous media is improving, there is a corresponding tradeoff in the size of the sample that can be investigated. This is a problem when one of the objectives is to upscale pore scale parameters and processes to the larger continuum scale. An even more significant challenge will be to develop and apply methods for chemical/mineralogical mapping in 3D—as discussed in this chapter, most of the chemical mapping methods are based on 2D geometries. There is also a need to further develop techniques that can span a significant range of spatial scales, particularly so as to be able to resolve the entire pore size distribution. Right now, SANS and USANS are probably the best techniques available, but they produce statistical data that can only be interpreted in terms of the 3D porous medium geometry using model assumptions. Without these new techniques, the nanoporosity within the subsurface sediment, which contributes so much in the way of reactivity to the porous medium, cannot be factored in.

To go with the advances in characterization, we need a new generation of pore scale models that scale efficiently on high performance computing frameworks. While the pore network models have already demonstrated their usefulness in analyzing pore scale dynamics, especially for multi-phase systems, there is a clear need for fully resolved pore scale models where this is possible. This implies that work on conceptual and computational models for pore scale physical and chemical processes, especially for the case of multi-phase flow characterizing CO₂

injection and sequestration, will continue. At the pore scale, there is a need (and even requirement) to be able to address full multicomponent chemistry, while resolving pore scale gradients in flow velocity, solute concentration, and reaction rates.

Probably the single most important process coupling that needs to be explored further is that between chemical and mechanical processes. The force of crystallization needs to be factored into pore scale models and the associated stress field. Conversely, the stress field needs to affect the thermodynamics and kinetics of the biogeochemical reaction networks. Further progress is also needed on the explicit incorporation of microbial communities into pore scale models, since these communities (which compete and collaborate) may regulate the overall chemistry (especially redox) of the subsurface system.

The upside here is that this approach has the potential to finally provide mechanistic explanations for many of the long-standing conundrums in reactive geochemistry in porous media, not least of which is the so-called discrepancy between laboratory and field rates. It is clear that the pore scale approach offers the chance to understand reaction-induced porosity, permeability, and reactivity change, although one still expects that molecular to nanometer scale effects will need to be integrated into the otherwise mesoscale (pore scale) studies. The combination of new microscopic characterization, experimental, and modeling approaches presents the opportunity for a new paradigm in the cross disciplinary fields of geochemistry, hydrology, and geophysics. Of course, this progress goes well beyond the narrower topic of subsurface CO₂ injection and sequestration and in fact will improve our understanding of water-rock interaction as a whole.

ACKNOWLEDGMENTS

This material is based upon work supported as part of the Center for Nanoscale Control of Geologic CO₂, an Energy Frontier Research Center funded by the US Department of Energy, Office of Science, Office of Basic Energy Sciences under Award No. DE-AC02-05CH11231. Additional support for the chapter preparation was provided by the Office of Basic Energy Sciences (Geosciences Program) of the U.S. Department of Energy. We are also grateful for the constructive reviews of the manuscript provided by Hongkyu Yoon, Christian Huber, and Ian Bourg.

REFERENCES

- Al-Fossail K, Handy LL (1990) Correlation between capillary number and residual water saturation. *J Colloid Interface Sci* 134:256-263
- Anovitz L, Cole D, Rother G, Allard L, Jackson A, Littrell K (2013) Diagenetic changes in macro- to nano-scale porosity in the St. Peter Sandstone: An (ultra) small angle neutron scattering and backscattered electron imaging analysis. *Geochim Cosmochim Acta* 102:280-305
- Appelo CAJ, Wersin P (2007) Multicomponent diffusion modeling in clay systems with application to the diffusion of tritium, iodide, and sodium in Opalinus clay. *Environ Sci Technol* 41:5002-5007
- Armstrong R, Ajo-Franklin J (2011) Investigating biomineralization using synchrotron based X-ray computed microtomography. *Geophys Res Lett* 38:L08406, doi: 10.1029/2011GL046916
- Armstrong RT, Porter ML, Wildenschild D (2012) Linking pore-scale interfacial curvature to column-scale capillary pressure. *Adv Water Resour* 46:55-62
- Audigane P, Gaus I, Czernichowski-Lauriol I, Pruess K, Xu T (2007) Two-dimensional reactive transport modeling of CO₂ injection in a saline aquifer at the Sleipner site, North Sea. *Am J Sci* 307:974-1008
- Balhoff M, Thomas S, Wheeler M (2008) Mortar coupling and upscaling of pore-scale models. *Comput Geosci* 12:15-27
- Bandara UC, Tartakovsky AM, Palmer BJ (2011) Pore-scale study of capillary trapping mechanism during CO₂ injection in geological formations. *Int J Greenhouse Gas Control* 5:1566-1577
- Battiatto I, Tartakovsky DM, Tartakovsky AM, Scheibe T (2011) Hybrid models of reactive transport in porous and fractured media. *Adv Water Resour* 34:1140-1150

- Bauer D, Youssef S, Fleury M, Bekri S, Rosenberg E, Vizika O (2012) Improving the estimations of petrophysical transport behavior of carbonate rocks using a dual pore network approach combined with computed microtomography. *Transport Porous Med* 94:505-524
- Bear J (1988) *Dynamics of Fluids in Porous Media*. Dover Books on Physics and Chemistry, Dover
- Benezeth P, Palmer DA, Anovitz LM, Horita J (2007) Dawsonite synthesis and reevaluation of its thermodynamic properties from solubility measurements: Implications for mineral trapping of CO₂. *Geochim Cosmochim Acta* 71:4438-4455
- Ben-Yaakov S (1972) Diffusion of sea water ions-I. Diffusion of sea water into a dilute solution. *Geochim Cosmochim Acta* 36:1395-1406
- Bhatnagar PL, Gross EP, Krook M (1954) A model for collision processes in gases. I. Small amplitude processes in charged and neutral one-component systems. *Phys Rev* 94:511-525
- Blunt MJ (2001) Flow in porous media - pore-network models and multiphase flow. *Curr Opin Colloid Interface Sci* 6:197-207
- Blunt MJ, Bijeljic B, Dong H, Gharbi O, Iglauer S, Mostaghimi P, Paluszny A, Pentland C (2013) Pore-scale imaging and modelling. *Adv Water Resour* 51:197-216
- Blunt MJ, Jackson MD, Piri M, Valvatne PH (2002) Detailed physics, predictive capabilities and macroscopic consequences for pore-network models of multiphase flow. *Adv Water Resour* 25:1069-1089
- Bogdanov I, Guerton F, Kpahou J, Kamp A (2011) Direct pore-scale modeling of two-phase flow through natural media. *In: Proceedings of the 2011 COMSOL Conference in Stuttgart*; http://www.comsol.com/paper/download/83497/bogdanov_paper.pdf
- Boschi C, Dini A, Dallai L, Ruggieri G, Gianelli G (2009) Enhanced CO₂-mineral sequestration by cyclic hydraulic fracturing and Si-rich fluid infiltration into serpentinites at Malenratra (Tuscany, Italy). *Chem Geol* 265:209-226
- Boudreau BP, Meysman FJ, Middelburg JJ (2004) Multicomponent ionic diffusion in porewaters: coulombic effects revisited. *Earth Planet Sci Lett* 222:653-666
- Bracco JN, Stack AG, Steeffel CI (2013) Upscaling calcite growth rates from the mesoscale to the macroscale. *Environ Sci Technol* 47:7555-7562
- Brimhall (1979) Lithologic determination of mass transfer mechanisms of multiple-stage porphyry copper mineralization at Butte, Montana; vein formation by hypogene leaching and enrichment of potassium-silicate protore. *Econ Geol* 74:556-589
- Brunauer S, Emmett PH, Teller E (1938) Adsorption of gases in multimolecular layers. *J Am Chem Soc* 60:309-319
- Burch T, Nagy K, Lasaga A (1993) Free energy dependence of albite dissolution kinetics at 80°C and pH 8.8. *Chem Geol* 105:137-162
- Cahn JW, Hilliard JE (1958) Free energy of a nonuniform system. I. Interfacial free energy. *J Chem Phys* 28:258-267
- Carlson WD (2006) Three-dimensional imaging of earth and planetary materials. *Earth Planet Sci Lett* 249:133-147
- Carroll SA, McNab WW, Dai Z, Torres SC (2013) Reactivity of Mount Simon sandstone and the Eau Claire shale under CO₂ storage conditions. *Environ Sci Technol* 47:252-261
- Chalraud C, Robin M, Lombard JM, Martin F, Egermann P, Bertin H (2009) Interfacial tension measurements and wettability evaluation for geological CO₂ storage. *Adv Water Resour* 32:98-109
- Chen C, Zhang D (2010) Pore-scale simulation of density-driven convection in fractured porous media during geological CO₂ sequestration. *Water Resour Res* 46:W11527, doi: 10.1029/2010WR009453
- Chen S, Doolen G (1998) Lattice Boltzmann method for fluid flows. *Annu Rev Fluid Mech* 30:329-364
- Chou L, Garrels R, Wollast R (1989) Comparative-study of the kinetics and mechanisms of dissolution of carbonate minerals. *Chem Geol* 78:269-282
- Cohen CE, Ding D, Quintard M, Bazin B (2008) From pore scale to wellbore scale: Impact of geometry on wormhole growth in carbonate acidization. *Chem Eng Sci* 63:3088-3099
- Crawshaw JP, Boek ES (2013) Multi-scale imaging and simulation of structure, flow and reactive transport for CO₂ storage and EOR in carbonate reservoirs. *Rev Mineral Geochem* 77:431-458
- Daccord G, Lenormand R, Liétard O (1993) Chemical dissolution of a porous medium by a reactive fluid-I. Model for the "wormholing" phenomenon. *Chem Eng Sci* 48:169-178
- Daval D, Martinez I, Corvisier J, Findling N, Goffe B, Guyot F (2009) Carbonation of Ca-bearing silicates, the case of wollastonite: Experimental investigations and kinetic modeling. *Chem Geol* 265:63-78
- de Gennes PG (1985) Wetting: statics and dynamics. *Rev Mod Phys* 57:827-863
- de Marsily G (1986) *Quantitative Hydrogeology: Groundwater Hydrology for Engineers*. Academic Press
- De Yoreo JJ, Vekilov PG (2003) Principles of crystal nucleation and growth. *Rev Mineral Geochem* 54:57-93
- De Yoreo JJ, Waychunas GA, Jun Y-S, Fernandez-Martinez A (2013) *In situ* investigations of carbonate nucleation on mineral and organic surfaces. *Rev Mineral Geochem* 77:229-257
- Deng H, Ellis BR, Peters CA, Fitts JP, Crandall D, Bromhal GS (2013) Modifications of carbonate fracture hydrodynamic properties by CO₂-acidified brine flow. *Energy Fuels* 27:4221-4231

- DePaolo DJ, Cole DR (2013) Geochemistry of geologic carbon sequestration: an overview. *Rev Mineral Geochem* 77:1-14
- Druhan JL, Steefel CI, Williams KH, DePaolo DJ (2013) Calcium isotope fractionation in groundwater: Molecular scale processes influencing field scale behavior. *Geochim Cosmochim Acta* 119:93-116
- Dutta T, Tarafdar S (2003) Fractal pore structure of sedimentary rocks: Simulation by ballistic deposition. *J Geophys Res-Solid Earth* 108(B2):2062, doi: 10.1029/2001JB000523
- Einstein A (1956) *Investigations on the Theory of the Brownian Movement*. R Firth, translated by AD Cowper, New York: Dover
- Elkhoury JE, Ameli P, Detwiler RL (2013) Dissolution and deformation in fractured carbonates caused by flow of CO₂-rich brine under reservoir conditions. *Int J Greenhouse Gas Control* 16, Supplement 1:S203-S215
- Ellis B, Peters C, Fitts J, Bromhal G, McIntyre D, Warzinski R, Rosenbaum E (2011) Deterioration of a fractured carbonate caprock exposed to CO₂-acidified brine flow. *Greenhouse Gases Sci Technol* 1:248-260
- Ellis JS, Bazylak A (2012) Dynamic pore network model of surface heterogeneity in brine-filled porous media for carbon sequestration. *Phys Chem Chem Phys* 14:8382-8390
- Ellis JS, Bazylak A (2013) Investigation of contact angle heterogeneity on CO₂ saturation in brine-filled porous media using 3D pore network models. *Energy Convers Manage* 68:253-259
- Er V, Babadagli T, Xu Z (2010) Pore-scale investigation of the matrix fracture interaction during CO₂ injection in naturally fractured oil reservoirs. *Energy Fuel* 24:1421-1430
- Ewing RP, Berkowitz B (1998) A generalized growth model for simulating initial migration of dense non-aqueous phase liquids. *Water Resour Res* 34:611-622
- Fatt I (1956) The network model of porous media. 1. Capillary pressure characteristics. *Petroleum Transactions, AIME* 207:144-159
- Feder J (1988) *Fractals, Physics of Solids and Liquids*. Springer
- Felmy AR, Weare JH (1991) Calculation of multicomponent ionic diffusion from zero to high concentration: I. The system Na-K-Ca-Mg-Cl-SO₄-H₂O at 25°C. *Geochim Cosmochim Acta* 55:113-131
- Fitts JP, Peters CA (2013) Caprock fracture dissolution and CO₂ leakage. *Rev Mineral Geochem* 77:459-479
- Flukiger F, Bernard D (2009) A new numerical model for pore scale dissolution of calcite due to CO₂ saturated water flow in 3D realistic geometry: Principles and first results. *Chem Geol* 265:171-180
- Fredd CN, Fogler HS (1998) Influence of transport and reaction on wormhole formation in porous media. *AIChE J* 44:1933-1949
- Gaus I, Audigane P, Andre L, Lions J, Jacquemet N, Durst P, Czernichowski-Lauriol I, Azaroual M (2008) Geochemical and solute transport modelling for CO₂ storage, what to expect from it? *Int J Greenh Gas Con* 2:605-625
- Gebrehiwet T, Redden G, Fujita Y, Beig M, Smith R (2012) The effect of the CO₂²⁻ to Ca²⁺ ion activity ratio on calcite precipitation kinetics and Sr²⁺ partitioning. *Geochim Trans* 13:1, doi: 10.1186/1467-4866-13-1
- Giambalvo ER, Steefel CI, Fisher AT, Rosenberg ND, Wheat CG (2002) Effect of fluid-sediment reaction on hydrothermal fluxes of major elements, eastern flank of the Juan de Fuca Ridge. *Geochim Cosmochim Acta* 66:173-1757
- Gonzalez R, Woods R (2008) *Digital Image Processing*. Pearson/Prentice Hall
- Gouze P, Luquot L (2011) X-ray microtomography characterization of porosity, permeability and reactive surface changes during dissolution. *J Contam Hydrol* 120-121:45-55
- Hamm LM, Bourg IC, Wallace AF, Rotenberg B (2013) Molecular simulation of CO₂- and CO₃-brine-mineral systems. *Rev Mineral Geochem* 77:189-228
- Hellevang H, Declercq J, Aagaard P (2011) Why is dawsonite absent in CO₂ charged reservoirs? *Oil Gas Sci Technol* 66:119-135
- Hellmann R, Tisserand D (2006) Dissolution kinetics as a function of the Gibbs free energy of reaction: An experimental study based on albite feldspar. *Geochim Cosmochim Acta* 70:364-383
- Hiorth A, Jettestuen E, Cathles L, Madland M (2013) Precipitation, dissolution, and ion exchange processes coupled with a lattice Boltzmann advection diffusion solver. *Geochim Cosmochim Acta* 104:99-110
- Hoefner ML, Fogler HS (1988) Pore evolution and channel formation during flow and reaction in porous media. *AIChE J* 34:45-54
- Huang H, Meakin P (2008) Three-dimensional simulation of liquid drop dynamics within unsaturated vertical Hele-Shaw cells. *Water Resour Res* 44: W03411, doi: 10.1029/2007WR006158
- Huang H, Meakin P, Liu M (2005) Computer simulation of two-phase immiscible fluid motion in unsaturated complex fractures using a volume of fluid method. *Water Resour Res* 41:W12413, doi: 10.1029/2005WR004204
- Hussain R, Pintelon T, Mitchell J, Johns M (2011) Using NMR displacement measurements to probe CO₂ entrapment in porous media. *AIChE J* 57:1700-1709
- Jamtveit B, Meakin P (1999) *Growth, Dissolution and Pattern Formation in Geosystems*. Springer
- Joekar-Niasar V, Hassanizadeh SM (2012) Analysis of fundamentals of two-phase flow in porous media using dynamic pore-network models: a review. *Crit Rev Env Sci Technol* 42:1895-1976

- Jun YS, Giammar DE, Werth CJ (2013) Impacts of geochemical reactions on geologic carbon sequestration. *Environ Sci Technol* 47:3-8
- Jung JW, Wan J (2012) Supercritical CO₂ and ionic strength effects on wettability of silica surfaces: equilibrium contact angle measurements. *Energy Fuel* 26:6053-6059
- Kang Q, Lichtner PC, Zhang D (2007) An improved lattice Boltzmann model for multicomponent reactive transport in porous media at the pore scale. *Water Resour Res* 43:W12S14, doi: 10.1029/2006WR005551
- Kang Q, Tsimpanogiannis IN, Zhang D, Lichtner PC (2005) Numerical modeling of pore-scale phenomena during CO₂ sequestration in oceanic sediments. *Fuel Process Technol* 86:1647-1665
- Kim D, Peters CA, Lindquist WB (2011) Upscaling geochemical reaction rates accompanying acidic CO₂-saturated brine flow in sandstone aquifers. *Water Resour Res* 47:W01505, doi: 10.1029/2010WR009472
- Kim Y, Wan J, Kneafsey TJ, Tokunaga TK (2012) Dewetting of silica surfaces upon reactions with supercritical CO₂ and brine: pore-scale studies in micromodels. *Environ Sci Technol* 46:4228-4235
- Kneafsey TJ, Silin D, Ajo-Franklin JB (2013) Supercritical CO₂ flow through a layered silica sand/calcite sand system: Experiment and modified maximal inscribed spheres analysis. *Int J Greenhouse Gas Control* 14:141-150
- Landrot G, Ajo-Franklin JB, Yang L, Cabrini S, Steefel CI (2012) Measurement of accessible reactive surface area in a sandstone, with application to CO₂ mineralization. *Chem Geol* 318-319:113-125
- Lasaga AC (1979) The treatment of multi-component diffusion and ion pairs in diagenetic fluxes. *Am J Sci* 279:324-346
- Lasaga A (1998) *Kinetic Theory in the Earth Sciences*. Princeton Series in Geochemistry. Princeton University Press
- Lasaga AC (1981) Transition State Theory. *Rev Mineral Geochem* 8:135-168
- Le Borgne T, Bolster D, Dentz M, de Anna P, Tartakovsky A (2011) Effective pore-scale dispersion upscaling with a correlated continuous time random walk approach. *Water Resour Res* 47:W12538, doi: 10.1029/2011WR010457
- Lenormand R, Touboul E, Zarcone C (1988) Numerical-models and experiments on immiscible displacements in porous-media. *J Fluid Mech* 189:165-187
- Li L, Steefel CI, Yang L (2008) Scale dependence of mineral dissolution rates within single pores and fractures. *Geochim Cosmochim Acta* 72:360-377
- Li X, Huang H, Meakin P (2008) Level set simulation of coupled advection-diffusion and pore structure evolution due to mineral precipitation in porous media. *Water Resour Res* 44:W12407, doi: 10.1029/2007WR00674
- Li X, Huang H, Meakin P (2010) A three-dimensional level set simulation of coupled reactive transport and precipitation/dissolution. *Int J Heat Mass Transfer* 53:2908-2923
- Lindquist W, Venkatarangan A (1999) Investigating 3D geometry of porous media from high resolution images. *Phys Chem Earth Part A* 24:593-599
- Lindquist WB, Venkatarangan A, Dunsmuir J, Wong Tf (2000) Pore and throat size distributions measured from synchrotron X-ray tomographic images of Fontainebleau sandstones. *J Geophys Res-Solid Earth* 105:21509-21527
- Liu C, Shang J, Zachara JM (2011) Multispecies diffusion models: A study of uranyl species diffusion. *Water Resour Res* 47:W12514, doi:10.1029/2011WR010575
- Luquot L, Gouze P (2009) Experimental determination of porosity and permeability changes induced by injection of CO₂ into carbonate rocks. *Chem Geol* 265:148-159
- Maher K, Steefel CI, DePaolo DJ, Viani BE (2006) The mineral dissolution rate conundrum: Insights from reactive transport modeling of U isotopes and pore fluid chemistry in marine sediments. *Geochim Cosmochim Acta* 70:337-363
- McGrail B, Schaeff H, Glezakova VA, Dang L, Owen A (2009) Water reactivity in the liquid and supercritical CO₂ phase: Has half the story been neglected? *Energy Procedia* 1:3415-3419
- Meakin P, Tartakovsky AM (2009) Modeling and simulation of pore-scale multiphase fluid flow and reactive transport in fractured and porous media. *Rev Geophys* 47:RG3002
- Mees F, Swennen R, Geet MV, Jacobs P (2003) Applications of X-ray computed tomography in the geosciences. *Geol Soc London Spec Publ* 215:1-6
- Mehmani Y, Sun T, Balhoff M, Eichhubl P, Bryant S (2012) Multiblock pore-scale modeling and upscaling of reactive transport: application to carbon sequestration. *Transport Porous Med* 95:305-326
- Miller G, Trebotich D (2012) An embedded boundary method for the Navier-Stokes equations on a time-dependent domain. *Commun Appl Math Comp Sci* 7:1-31
- Molins S, Silin D, Trebotich D, Steefel CI (2011) Direct pore-scale numerical simulation of precipitation and dissolution. *Mineral Mag* 75:1487
- Molins S, Trebotich D, Shen C, Yang L, Ajo-Franklin J, Steefel C (2012) Calcite dissolution driven by a CO₂-rich solution in a flow-through capillary tube: experiment and pore-scale modeling. Abstract H52C-06 presented at 2012 Fall Meeting AGU, San Francisco, Calif. 3-7 Dec.

- Molins S, Trebotich D, Steefel CI, Shen C (2012) An investigation of the effect of pore scale flow on average geochemical reaction rates using direct numerical simulation. *Water Resour Res* 48:W03527, doi:10.1029/2011WR011404
- Muller N, Qi R, Mackie E, Pruess K, Blunt MJ (2009) CO₂ injection impairment due to halite precipitation. *Energy Procedia* 1:3507-3514
- Nehrke G, Reichart G, Cappellen PV, Meile C, Bijma J (2007) Dependence of calcite growth rate and Sr partitioning on solution stoichiometry: Non-Kossel crystal growth. *Geochim Cosmochim Acta* 71:2240-2249
- Nielsen LC, Bourg IC, Sposito G (2012) Predicting CO₂-water interfacial tension under pressure and temperature conditions of geologic CO₂ storage. *Geochim Cosmochim Acta* 81:28-38
- Noiriel C, Guze P, Bernard D (2004) Investigation of porosity and permeability effects from microstructure changes during limestone dissolution. *Geophys Res Lett* 31:L24603
- Noiriel C, Luquot L, Madé B, Raimbault L, Guze P, van der Lee J (2009) Changes in reactive surface area during limestone dissolution: An experimental and modelling study. *Chem Geol* 265:160-170
- Noiriel C, Steefel CI, Yang L, Ajo-Franklin J (2012) Upscaling calcium carbonate precipitation rates from pore to continuum scale. *Chem Geol* 318-319:60-74
- Ortoleva P (1994) *Geochemical Self-Organization*. Oxford University Press
- Ortoleva P, Chadam J, Merino E, Sen A (1987) Geochemical self-organization II; the reactive-infiltration instability. *Am J Sci* 287:1008-1040
- Ovaysi S, Piri M (2013) Pore-scale dissolution of CO₂+SO₂ in deep saline aquifers. *Int J Greenhouse Gas Control* 15:119-133
- Parmigiani A, Huber C, Bachmann O, Chopard B (2011) Pore-scale mass and reactant transport in multiphase porous media flows. *J Fluid Mech* 686:40-76
- Patankar S (1980) *Numerical Heat Transfer and Fluid Flow*, Series in Computational Methods in Mechanics and Thermal Sciences. Taylor & Francis
- Payatakes AC, Tien C, Turian RM (1973) A new model for granular porous media: Part I. Model formulation. *AIChE J* 19:58-67
- Peters CA (2009) Accessibilities of reactive minerals in consolidated sedimentary rock: An imaging study of three sandstones. *Chem Geol* 265:198-208
- Phillips O (1991) *Flow and Reactions in Permeable Rocks*. Cambridge University Press
- Pini R, Benson SM (2013) Simultaneous determination of capillary pressure and relative permeability curves from core-flooding experiments with various fluid pairs. *Water Resour Res* 49:3516-3530, doi: 10.1002/wrcr.20274
- Plummer L, Wigley T, Parkhurst D (1978) Kinetics of calcite dissolution in CO₂-Water systems at 5°C to 60°C and 0.0 to 1.0 atm CO₂. *Am J Sci* 278:179-216
- Pokrovsky OS, Golubev SV, Schott J (2005) Dissolution kinetics of calcite, dolomite and magnesite at 25 °C and 0 to 50 atm pCO₂. *Chem Geol* 217:239-255
- Pokrovsky OS, Golubev SV, Schott J, Castillo A (2009) Calcite, dolomite and magnesite dissolution kinetics in aqueous solutions at acid to circumneutral pH, 25 to 150°C and 1 to 55 atm pCO₂: New constraints on CO₂ sequestration in sedimentary basins. *Chem Geol* 265:20-32
- Prigogine I (1968) *Introduction to Thermodynamics of Irreversible Processes*. Interscience Publishers
- Prigogine I (1980) *From Being to Becoming: Time and Complexity in the Physical Sciences*. W H Freeman & Company
- Pudney C (1998) Distance-ordered homotopic thinning: a skeletonization algorithm for 3D digital images. *Comput Vision Image Understanding* 72:404-413
- Racini AQ, Blunt MJ, Bijeljic B (2012) Modelling two-phase flow in porous media at the pore scale using the volume-of-fluid method. *J Comput Phys* 231:5653-5668
- Rolle M, Muniruzzaman M, Haberer CM, Grathwohl P (2013) Coulombic effects in advection-dominated transport of electrolytes in porous media: Multicomponent ionic dispersion. *Geochim Cosmochim Acta* 120:195-205
- Sadhukhan S, Guze P, Dutta T (2012) Porosity and permeability changes in sedimentary rocks induced by injection of reactive fluid: A simulation model. *J Hydrol* 450-451:134-139
- Saldi GD, Schott J, Pokrovsky OS, Gautier Q, Oelkers EH (2012) An experimental study of magnesite precipitation rates at neutral to alkaline conditions and 100-200 °C as a function of pH, aqueous solution composition and chemical affinity. *Geochim Cosmochim Acta* 83:93-109
- Sato K, Mito S, Horie T, Ohkuma H, Saito H, Watanabe J, Yoshimura T (2011) Monitoring and simulation studies for assessing macro- and meso-scale migration of {CO₂} sequestered in an onshore aquifer: Experiences from the Nagaoka pilot site, Japan. *Int J Greenhouse Gas Control* 5:125-137
- Scheibe TD, Hou Z, Palmer BJ, Tartakovsky AM (2013) Pore-scale simulation of intragranular diffusion: Effects of incomplete mixing on macroscopic manifestations. *Water Resour Res* 49:4277-4294, doi: 10.1002/wrcr.20333

- Scheibe TD, Tartakovsky AM, Tartakovsky DM, Redden GD, Meakin P (2007) Hybrid numerical methods for multiscale simulations of subsurface biogeochemical processes. *J Phys Conf Ser* 78:012063
- Shan X, Doolen G (1995) Multicomponent lattice-Boltzmann model with interparticle interaction. *J Stat Phys* 81:379-393
- Silin D, Patzek T (2006) Pore space morphology analysis using maximal inscribed spheres. *Physica A* 371:336-360
- Silin D, Tomutsa L, Benson S, Patzek T (2011) Microtomography and pore-scale modeling of two-phase fluid distribution. *Transport Porous Med* 86:495-515
- Smith MM, Sholokhova Y, Hao Y, Carroll SA (2013) Evaporite caprock integrity: an experimental study of reactive mineralogy and pore-scale heterogeneity during brine-CO₂ exposure. *Environ Sci Technol* 47:262-268
- Smith MM, Wolery TJ, Carroll SA (2013) Kinetics of chlorite dissolution at elevated temperatures and CO₂ conditions. *Chem Geol* 347:1-8
- Stauffer D, Adler J, Aharony A (1994) Universality at the three-dimensional percolation threshold. *J Phys A* 27:L475
- Steeffel C, Lichtner P (1998) Multicomponent reactive transport in discrete fractures: II: Infiltration of hyperalkaline groundwater at Maqarin, Jordan, a natural analogue site. *J Hydrol* 209:200-224
- Steeffel CI, DePaolo DJ, Lichtner PC (2005) Reactive transport modeling: An essential tool and a new research approach for the Earth sciences. *Earth Planet Sci Lett* 240:539-558
- Steeffel CI, Lasaga AC (1990) Evolution of dissolution patterns: Permeability change due to coupled flow and reaction. *In: Chemical Modeling of Aqueous Systems II*. ACS Symposium Series 416:212-225
- Steeffel CI, Lasaga AC (1994) A coupled model for transport of multiple chemical species and kinetic precipitation/dissolution reactions with application to reactive flow in single phase hydrothermal systems. *Am J Sci* 294:529-592
- Steeffel CI, Lichtner PC (1994) Diffusion and reaction in rock matrix bordering a hyperalkaline fluid-filled fracture. *Geochim Cosmochim Acta* 58:3595-3612
- Steeffel CI, Maher K (2009) Fluid-rock interaction: A reactive transport approach. *Rev Mineral Geochem* 70:485-532
- Suekane T, Furukawa N, Tsushima S, Hirai S, Kiyota M (2009) Application of MRI in the measurement of two-phase flow of supercritical CO₂ and water in porous rocks. *J Porous Med* 12:143-154
- Suekane T, Soukawa S, Iwatani S, Tsushima S, Hirai S (2005) Behavior of supercritical CO₂ injected into porous media containing water. *Energy* 30:2370-2382
- Tartakovsky AM, Meakin P, Scheibe TD, West RME (2007) Simulations of reactive transport and precipitation with smoothed particle hydrodynamics. *J Comput Phys* 222:654-672
- Tartakovsky AM, Meakin P, Scheibe TD, Wood BD (2007) A smoothed particle hydrodynamics model for reactive transport and mineral precipitation in porous and fractured porous media. *Water Resour Res* 43:W05437
- Tartakovsky AM, Redden G, Lichtner PC, Scheibe TD, Meakin P (2008) Mixing-induced precipitation: Experimental study and multiscale numerical analysis. *Water Resour Res* 44:W06S04, doi: 10.1029/2006WR005725
- Taylor G (1953) Dispersion of soluble matter in solvent flowing slowly through a tube. *Proc Roy Soc Lond Ser-A* 219:186-203
- Teng H, Dove PM, Yoreo JJD (2000) Kinetics of calcite growth: surface processes and relationships to macroscopic rate laws. *Geochim Cosmochim Acta* 64:2255-2266
- Tokunaga TK, Wan J (2013) Capillary pressure and mineral wettability influences on reservoir CO₂ capacity. *Rev Mineral Geochem* 77:481-503
- Trebotich D, Straalen BV, Graves D, Colella P (2008) Performance of embedded boundary methods for CFD with complex geometry. *J Phys Conf Ser* 125:012083
- Van Cappellen P, Gaillard JF (1996) Biogeochemical dynamics in aquatic sediments. *Rev Mineral* 34:335-376
- Varloteaux C, Bekri S, Adler PM (2013) Pore network modeling to determine the transport properties in presence of a reactive fluid: From pore to reservoir scale. *Adv Water Resour* 53:87-100
- Wang Y, Zhang C, Wei N, Oostrom M, Wietsma TW, Li X, Bonneville A (2013) Experimental study of crossover from capillary to viscous fingering for supercritical CO₂-water displacement in a homogeneous pore network. *Environ Sci Technol* 47:212-218
- Wigley M, Kampman N, Dubacq B, Bickle M (2012) Fluid-mineral reactions and trace metal mobilization in an exhumed natural CO₂ reservoir, Green River, Utah. *Geology* 40:555-558
- Wildenschild D, Sheppard AP (2013) X-ray imaging and analysis techniques for quantifying pore-scale structure and processes in subsurface porous medium systems. *Adv Water Resour* 51:217-246
- Wolery T, Jackson K, Bourcier W, Bruton C, Viani B, Knauss K, Delany J (1990) Chemical Modeling of Aqueous Systems II, chap. Current status of the EQ3/6 software package for geochemical modeling. *In: Chemical Modeling of Aqueous Systems II*. ACS Symposium Series 416:104-116

- Wolthers M, Nehrke G, Gustafsson JP, Cappellen PV (2012) Calcite growth kinetics: Modeling the effect of solution stoichiometry. *Geochim Cosmochim Acta* 77:121-134
- Xu Z, Meakin P (2008) Phase-field modeling of solute precipitation and dissolution. *J Chem Phys* 129:014705, <http://dx.doi.org/10.1063/1.2948949>
- Xu Z, Meakin P (2011) Phase-field modeling of two-dimensional solute precipitation/dissolution: Solid fingers and diffusion-limited precipitation. *J Chem Phys* 134:044137
- Xu Z, Meakin P, Tartakovsky AM (2009) Diffuse-interface model for smoothed particle hydrodynamics. *Phys Rev E* 79:036702
- Yang L, Steefel CI (2008) Kaolinite dissolution and precipitation kinetics at 22 C and pH 4. *Geochim Cosmochim Acta* 72:99-116
- Yoon H, Dewers TA (2013) Nanopore structures, statistically representative elementary volumes, and transport properties of chalk. *Geophys Res Lett* 40, doi:10.1002/grl.50803
- Yoon H, Valocchi AJ, Werth CJ, Dewers T (2012) Pore-scale simulation of mixing-induced calcium carbonate precipitation and dissolution in a microfluidic pore network. *Water Resour Res* 48
- Zhang C, Oostrom M, Grate JW, Wietsma TW, Warner MG (2011) Liquid CO₂ displacement of water in a dual-permeability pore network micromodel. *Environ Sci Technol* 45:7581-7588
- Zienkiewicz O, Taylor R, Zhu J (2005) *The Finite Element Method: Its Basis and Fundamentals: Its Basis and Fundamentals*. Elsevier Science